Relating cloud and aerosol properties from long-term lidar observations in Tajikistan

Leipzig Institute of Meteorology
Faculty of Physics and Earth Science
Leipzig University

Master Thesis

Friederike Lipken

Primary Reviewer: Prof. Dr. Andreas Macke

Secondary Reviewer: Prof. Dr. Johannes Quaas

Advisors: Dr. Julian Hofer and Dr. Cristofer Jimenez

Leipzig, 28 May 2024

Contents

1 Introduction **3**

2 Instruments and methods **7**
2.1 Lidar theory 7
2.1.1 Retrieval of aerosol optical properties 9
2.2 The PollyXT lidar system 12
2.3 PollyNET Processing Chain 15
2.3.1 High-temporal-resolution products 16
2.4 Aerosol particle, cloud and air mass characterization 17
2.4.1 Retrieval of microphysical and cloud-relevant properties 17
2.4.2 Dual-Field-of-View depolarization method 19
2.4.3 Analysis scheme 24
2.4.4 Aerosols and clouds in Tajikistan 27
2.4.5 Time-height resolved air mass source attribution tool . 29
2.5 Model-reanalysis-retrieved CCN concentrations 31
2.6 Spaceborne-lidar-retrieved CCN concentrations 32

3 Results **33**
3.1 Long-term statistical analysis 33
3.1.1 Seasonality of aerosol, clouds and meteorological situation 34
3.1.2 Aerosol-cloud interaction index 36
3.1.3 Seasonal air mass source attribution 41
3.2 Case Studies 44
3.2.1 Case 1: 17 October 2019 44
3.2.2 Case 2: 8–10 October 2019 51
3.2.3 Case 3: 1 June 2023 54
3.3 Comparison with CALIPSO- and CAMS-retrieved CCN number concentrations 58

4 Summary and Outlook **61**

A Uncertainties **64**

Chapter 1

Introduction

Clouds play a key role in the Earth's atmospheric dynamics, as they interact with both solar and terrestrial radiation, cause precipitation, and transport heat (Voigt et al., 2021). Despite their significant influence on the planet's radiation budget and water cycle, clouds remain the greatest source of uncertainty in assessing future climate, as the IPCC (Intergovernmental Panel on Climate Change) acknowledges (IPCC, 2014). Their complicated internal mechanisms and microphysical properties are closely connected to local atmospheric conditions, with aerosol particles playing a fundamental role in the formation, development, and lifetime of clouds.
Aerosols have a direct effect on radiation through scattering and absorption. Under favorable atmospheric conditions, some particles can act as cloud condensation nuclei (CCN) or ice nucleating particles (INP), which initiate cloud formation and therefore indirectly influence radiation and the hydrological cycle. Aerosol amount and compositions, meteorological conditions such as relative humidity and updraft (e.g., Reutter et al., 2009; Jimenez, 2021), and cloud formation processes are spatially and temporally versatile (Novakov and Penner, 1993). Therefore, clouds, aerosols, and their interactions, need to be resolved in the context of their environment. Ground-based active remote sensing approaches have shown potential in this matter given their ability to monitor aerosol and clouds simultaneously (Jimenez, 2021).
This thesis aims to delve into the topic by means of a state-of-the-art ground-based lidar, located in Dushanbe, Tajikistan (38° 33′ 34″ N, 68° 51′ 22″ E), which provides relevant information about aerosol and clouds, such as the concentration of water droplets in the cloud-base region (Jimenez et al., 2020a) and the concentration of potential CCN in the cloud surroundings (e.g., Hofer, 2020; Mamouri and Ansmann, 2016). The observatory located at 864 m a.s.l. at the S.U. Umarov Physical Technical Institute of the Academy of Sciences of the Republic of Tajikistan in partnership with the Leibniz In-

Figure 1.1: Map of dust belt (enclosed in green dashed line) with desert regions (black text), dust belt (bright), and Dushanbe, Tajikistan (marked with red star), adapted from Hofer (2020).

stitute for Tropospheric Research in Leipzig (TROPOS), Germany, is one of the few experimental measurement sites in this region (Hofer, 2020). The country is located within the dust belt (Fig. 1.1 Hofer, 2020), which reaches from the north-west African desert Sahara to the Gobi desert in Northeast Asia, containing regions that are affected by dust and dust storms. Additionally, to the desertification and the glacier retreat that are taking place within Tajikistan (e.g., Jiang et al., 2019; Goerlich et al., 2020), the desertification of surrounding areas also represent great potential of dust sources (e.g., Jiang et al., 2019; Goerlich et al., 2020). One example is the drying out of the Aral Sea which now has mostly become the Aralkum which translates to Aral desert (Abuduwaili et al., 2018). Local efforts are being made in investigating atmospheric processes, but most studies are restricted to satellite-based measurements (e.g., Liu et al., 2019; Rupakheti et al., 2019; Wang et al., 2020; Wu et al., 2022; Gan et al., 2024), which show, despite their great value, limitations regarding vertical high-resolved aerosol and cloud measurements at cloud-base and below clouds (Jimenez, 2021). In 2015–2016, first continuous lidar measurements were conducted in Dushanbe (Hofer et al., 2017). The 18-month campaign allowed the first long-term assessment of the aerosol situation in Dushanbe. In 2019, a new and upgraded permanent lidar station, now with Dual-Field-of-View capabilities, was deployed in Dushanbe (Engelmann et al., 2019; Jimenez et al., 2020b). The Dual-Field-of-View (DFOV) polarization method extends the capabilities of a lidar to assess microphysi-

cal information not only of aerosols (Mamouri and Ansmann, 2016) but also from activated droplets in real liquid water clouds in the continental-arid climate of Dushanbe, a location mostly influenced by pollution and dust. The continuous, long-term high-resolution measurements from 2019 to 2023 are subject of this study and were used to investigate the aerosol and cloud microphysical properties and their interactions in Dushanbe, Tajikistan.

Since the climate is changing due to anthropogenic influences, and the biosphere and other parts of the climate system are changing accordingly, continuous, mature knowledge about human-climate interaction is essential in order to understand the consequences of this change. Regarding aerosol-cloud interactions, Dushanbe itself, characterized by its continental, dusty, and often polluted conditions, offers an attractive scenario to study the primary aerosol-cloud relationship, commonly related to the Twomey effect (Twomey, 1974; Quaas et al., 2022) and is of essential character to assess further adjustments that affect cloud coverage and lifetime (Gryspeerdt et al., 2019).

Satellite observations have provided valuable knowledge regarding aerosol-cloud interactions, providing quantitative assessments of the Twomey effect (Quaas et al., 2006, 2008) and have set a path to evaluate the the adjustments by means of the cloud fraction and liquid-water path (Gryspeerdt et al., 2019). The coarse resolution of spaceborne observations often suits to climate scales, but the aerosol-cloud processes that occur in shorter temporal scales cannot be addressed. Airborne in situ measurements have been used to tackle shorter scales (Werner et al., 2014), but such measurements are limited in time and quantity. Ground-based lidar, on the other hand, can vertically resolve one location spot continuously and over long periods, and the recent developments into the lidar system and into the analysis chain open the chance to approach the experimental gap from the short to long time scales.

In this context, (Jimenez et al., 2020b,a) extended the Dual-Field-of-View concept initiated by Schmidt et al. (2013) towards depolarization, allowing the assessment of cloud properties during day and night time and with temporal resolutions of a few minutes. Such lidar systems are located at multiple regions across the globe, including the continental semi-arid environment of Dushanbe, Tajikistan.

The first lidar measurements in 2015–2016 in Dushanbe at the Physical Technical Institute of Tajikistan initially focused on aerosol properties and their cloud-relevant information such as the concentration of potential CCN and INP (Hofer et al., 2017). The extension to DFOV polarization lidar and the capacity to measure cloud microphysical properties enabled the first short-term results on aerosol-cloud-interaction to be obtained, which Jimenez (2021) evaluated. The present thesis deals with the data of the longer time

period from 2019–2023, covering about 28 months of measurements, with a focus on aerosol-cloud interactions and their properties in Dushanbe.
The thesis is structured starting with Chapter 2, which deals with the theoretical basis of lidar technology and describes the instrument specifications, methodological framework, and data analysis procedures. Chapter 3 presents the core analysis based on the obtained aerosol-cloud properties. Three case studies are discussed in detail and the aerosol-cloud relationship was evaluated by means of the aerosol-cloud-interaction index by consideration of environmental conditions and the temporal scale. To broaden the view of the aerosol situation, a comparison with recent datasets from spaceborne lidar and model outputs was performed. Finally, a summary and an outlook are provided to emphasize the importance of ongoing research for the understanding of the aerosol-cloud problem.

Chapter 2

Instruments and methods

This work aims to investigate aerosol-cloud interactions (ACI) in the Central Asian region. The PollyXT (POrtabLe Lidar sYstem PollyXT Althausen et al., 2009) system is measuring since 2019 in Dushanbe, Tajikistan, and the continuous vertical information that it provides form the base of this study.
First, this chapter covers the fundamentals of the lidar theory, the PollyXT lidar system, and the automated data processing chain PollyNET (Portable Lidar NETwork). Afterwards, methods to analyze aerosol, cloud, and air mass properties are described. The strategy to investigate the relationship between aerosol and cloud properties is then presented.

2.1 Lidar theory

A lidar (LIght Detection And Ranging) is an active instrument based on the emission of a laser beam and the detection of scattered light in the atmosphere. It emits a linearly polarized laser pulse at selected wavelengths into the atmosphere. The laser beam will be scattered by air molecules and particles like aerosols and hydrometeors. The light scattered in the backward direction is detected by a telescope as part of the receiving unit of the lidar. The power $P(R,\lambda)$ of the detected photons depends on the wavelength λ of the emitted laser beam and is a function of distance R between the receiver of the lidar and the atmospheric component that scattered the light back. This distance R can be calculated with the speed of light c and the travel time t of the two-way trip of the photons:

$$R = \frac{ct}{2} \,. \tag{2.1}$$

Then, the received power *P(R,λ)* for elastic backscattered signals can be described as follows (Weitkamp, 2005):

$$P\left(R,\lambda\right)=P_0\frac{O_\lambda\left(R\right)}{R^2}C_{\mathrm{s}}\left(\lambda\right)\beta_\lambda\left(R\right)\exp\left\{-2\int_0^R\alpha_\lambda\left(r\right)\mathrm{d}r\right\}\ , \tag{2.2}$$

where P_0 is the power of the emitted laser beam, $O_\lambda(R)$ accounts for the overlap of the laser beam and receiver field of view, C_s is the system constant to consider the efficiency of the detection, $\beta_\lambda(R)$ is the volume backscatter coefficient, which describes how much light is scattered back and can be described by means of particle and molecular contribution:

$$\beta_\lambda\left(R\right)=\beta_\lambda^{\mathrm{par}}\left(R\right)+\beta_\lambda^{\mathrm{mol}}\left(R\right)\ . \tag{2.3}$$

The volume extinction coefficient $\alpha_\lambda(r)$, when integrated over the range r from the lidar to the atmospheric component that scattered the light back, represents the attenuated light (Beer-Lamber-Bouguer law). The volume extinction coefficient can also be divided into particle and molecular parts:

$$\alpha_\lambda\left(r\right)=\alpha_\lambda^{\mathrm{par}}\left(r\right)+\alpha_\lambda^{\mathrm{mol}}\left(r\right). \tag{2.4}$$

In order to determine particle properties, the lidar equation must be solved for the two unknown properties α_λ and β_λ. For this purpose, the Klett or Raman method can be applied. Although the Klett method allows high temporal and spatial resolution during day and night, it requires an assumption of the lidar ratio S_λ. This ratio between particle extinction and backscatter coefficient is defined as:

$$S_\lambda\left(R\right)=\frac{\alpha_\lambda\left(R\right)}{\beta_\lambda\left(R\right)}. \tag{2.5}$$

To avoid the assumption of the lidar ratio the Raman method is introduced. For the Raman retrieval of particle properties the inelastic backscattering of Nitrogen molecules is utilized, and an additional equation for the received power can be expressed (Ansmann et al., 1990):

$$P\left(R,\lambda_{\mathrm{ra}}\right)=P_0\frac{O_\lambda\left(R\right)}{R^2}C_{\mathrm{s}}\left(\lambda\right)\beta_{\lambda_{\mathrm{ra}}}\left(R\right)\exp\left\{-\int_0^R\left[\alpha_\lambda\left(r\right)+\alpha_{\lambda_{\mathrm{ra}}}\left(r\right)\right]\mathrm{d}r\right\}\ , \tag{2.6}$$

where λ_{ra} is the Raman-shifted wavelength. The volume extinction coefficient at the Raman-shifted wavelength $\alpha_{\lambda_{\mathrm{ra}}}(r)$ is again containing particle and molecular parts and the Raman-shifted backscatter coefficient $\beta_{\lambda_{\mathrm{ra}}}(r)$ is described as:

$$\beta_{\lambda_{\mathrm{ra}}}\left(R\right)=N_{\mathrm{ra}}\left(R\right)\frac{d\sigma\left(\pi,\lambda_{\mathrm{ra}}\right)}{d\Omega}\ , \tag{2.7}$$

where $N_{\mathrm{ra}}(R)$ is the molecule number density of the Raman-active gas, which can be calculated from temperature and pressure profiles (Bucholtz, 1995). The second part of the equation describes the range-independent differential Raman backscatter cross section. These equations allow an independent calculation of the particle extinction and backscatter coefficients, which is described in Sect. 2.1.1.

2.1.1 Retrieval of aerosol optical properties

Based on Eq. 2.6 for elastic and inelastic backscattering, the particle extinction coefficient $\alpha_{\lambda}^{\mathrm{par}}$ can be calculated as follows (Ansmann et al., 1990):

$$\alpha_{\lambda}^{\mathrm{par}}(R) = \frac{\frac{\mathrm{d}}{dR}\ln\left[\frac{N_{\mathrm{ra}}(R)O_{\lambda}(R)}{R^2 P(R,\lambda_{\mathrm{ra}})}\right] - \alpha_{\lambda}^{\mathrm{mol}}(R) - \alpha_{\lambda_{\mathrm{ra}}}^{\mathrm{mol}}(R)}{1+\left(\frac{\lambda}{\lambda_{\mathrm{ra}}}\right)^{\mathring{a}(R)}} . \tag{2.8}$$

To calculate the particle backscatter coefficient $\beta_{\lambda}{}^{par}(r)$, the Eqs. 2.2 and 2.6 are combined (Ansmann et al., 1992a,b):

$$\begin{aligned}\beta_{\lambda}^{\mathrm{par}}(R) = &- \beta_{\lambda}^{\mathrm{mol}}(R) + [\beta_{\lambda}^{\mathrm{par}}(R_0) + \beta_{\lambda}^{\mathrm{mol}}(R_0)] \\ &\cdot \frac{P(R_0,\lambda_{\mathrm{ra}})P(R,\lambda)}{P(R_0,\lambda)P(R,\lambda_{\mathrm{ra}})} \cdot \frac{N_{\mathrm{ra}}(R)}{N_{\mathrm{ra}}(R_0)} \\ &\cdot \frac{\exp\left\{-\int_{R_0}^{R}[\alpha_{\lambda_{\mathrm{ra}}}^{\mathrm{par}}(r) + \alpha_{\lambda_{\mathrm{ra}}}^{\mathrm{mol}}(r)]\mathrm{d}r\right\}}{\exp\left\{-\int_{R_0}^{R}[\alpha_{\lambda}^{\mathrm{par}}(r) + \alpha_{\lambda}^{\mathrm{mol}}(r)]\mathrm{d}r\right\}} .\end{aligned} \tag{2.9}$$

For this calculation, a reference height R_0, where almost particle free conditions can be assumed, must be chosen and a generic small particle backscatter coefficient value at that reference height ($\beta_{\lambda}^{\mathrm{par}}(R_0)$) has to be set.
Based on the retrieved particle extinction and backscatter coefficient the particle lidar ratio can be calculated, which is defined as:

$$S_{\lambda}^{\mathrm{par}}(R) = \frac{\alpha_{\lambda}^{\mathrm{par}}(R)}{\beta_{\lambda}^{\mathrm{par}}(R)} . \tag{2.10}$$

Depolarization ratio

For the polarization lidar, additional equations, which describe the power that is received at the optical channel for parallel polarization ($\|$) and at

the optical channel for perpendicular polarization ($\perp$), as these components of the light are distinguished with an adjusted polarizer, can be stated as follows (e.g., Hofer, 2020):

$$^{\parallel}P\left(R,\lambda\right) = {}^{\parallel}P_0 \frac{^{\parallel}O_\lambda\left(R\right)}{R^2}\, {}^{\parallel}C_s\left(\lambda\right)^{\parallel}\beta_\lambda\left(R\right)\exp\left\{-2\int_0^R {}^{\parallel}\alpha_\lambda\left(r\right)\mathrm{d}r\right\} \tag{2.11}$$

and

$$^{\perp}P\left(R,\lambda\right) = {}^{\parallel}P_0 \frac{^{\perp}O_\lambda\left(R\right)}{R^2}\, {}^{\perp}C_s\left(\lambda\right)^{\perp}\beta_\lambda\left(R\right)\exp\left\{-\int_0^R \left[{}^{\parallel}\alpha_\lambda\left(r\right) + {}^{\perp}\alpha_\lambda\left(r\right)\right]\mathrm{d}r\right\} . \tag{2.12}$$

From these equations, the change of polarization due to atmospheric components based on the shape-induced scattering can be determined. This change is represented by the volume linear depolarization ratio $\delta_\lambda^{\mathrm{vol}}$ defined as:

$$\delta_\lambda^{\mathrm{vol}} = \frac{^{\perp}\beta_\lambda(R)}{^{\parallel}\beta_\lambda(R)} = \frac{^{\perp}\beta_\lambda^{\mathrm{par}}(R) + {}^{\perp}\beta_\lambda^{\mathrm{mol}}(R)}{^{\parallel}\beta_\lambda^{\mathrm{par}}(R) + {}^{\parallel}\beta_\lambda^{\mathrm{mol}}(R)} , \tag{2.13}$$

with the particle linear depolarization ratio $\delta_\lambda^{\mathrm{par}}$:

$$\delta_\lambda^{\mathrm{par}} = \frac{^{\perp}\beta_\lambda^{\mathrm{par}}(R)}{^{\parallel}\beta_\lambda^{\mathrm{par}}(R)} \tag{2.14}$$

and the molecular linear depolarization ratio $\delta_\lambda^{\mathrm{mol}}$:

$$\delta_\lambda^{\mathrm{mol}} = \frac{^{\perp}\beta_\lambda^{\mathrm{mol}}(R)}{^{\parallel}\beta_\lambda^{\mathrm{mol}}(R)} . \tag{2.15}$$

For the PollyXT lidar system, which measures the total and perpendicular polarization components, the volume depolarization ratio can be calculated as follows:

$$\delta_\lambda^{\mathrm{vol}}\left(R\right) = \frac{1 - \delta_\lambda^{'}\left(R\right)/V_\lambda^*}{\delta_\lambda^{'}\left(R\right)\cdot D_\lambda^{\mathrm{tot}}/V_\lambda^* - D_\lambda^{\perp}} \tag{2.16}$$

with

$$\delta_\lambda^{'}\left(R\right) = \frac{^{\perp}P\left(R,\lambda\right)}{P\left(R,\lambda\right)} . \tag{2.17}$$

Here, D_λ denotes the transmission ratio for the total and the perpendicular-polarized channels. In order to calculate these transmission ratios, calibration measurements were performed (Mattis et al., 2009; Hofer, 2020). The calibration constant V^* is calculated with the $\Delta 90°$-method (Freudenthaler

et al., 2009; Freudenthaler, 2016; Freudenthaler et al., 2018) and is defined as:

$$\mathrm{V}^*_\lambda(R) = \frac{1 + D^{\mathrm{tot}}_\lambda}{1 + D^{\perp}_\lambda} \sqrt{{}^{+45}\delta'_\lambda(R) \cdot {}^{-45}\delta'_\lambda(R)} \ . \tag{2.18}$$

For the $\Delta 90°$-method, calibration measurements are conducted at $+45°$ (${}^{+45}\delta'_\lambda(R)$) and $-45°$ (${}^{-45}\delta'_\lambda(R)$) in relation to the laser polarization plane. The calibration constant V^* represents the ratio of transmission through the optics of the two channels, which may vary over time e.g.,, due to a decrease in detector efficiency of one of the channels. Therefore, periodic calibration measurements are conducted.
Then, the particle linear depolarization ratio can be calculated as follows (e.g., Tesche et al., 2009):

$$\delta^{\mathrm{par}}_\lambda(R) = \left[\delta^{\mathrm{vol}}_\lambda(R) + 1\right] \left(\frac{\beta^{\mathrm{mol}}_\lambda(R) \left[\delta^{\mathrm{mol}}_\lambda(R) - \delta^{\mathrm{vol}}_\lambda(R)\right]}{\beta^{\mathrm{par}}_\lambda(R) \left[1 + \delta^{\mathrm{mol}}_\lambda(R)\right]} + 1 \right)^{-1} - 1 \ . \tag{2.19}$$

Ångström exponent

The wavelength dependence of optical parameters like extinction and backscatter is described by the Ångström exponent (e.g., Hofer, 2020). Based on pairs of particle backscatter coefficients at the emitted wavelengths 355 nm, 532 nm, and 1064 nm the backscatter-related Ångström exponent can be calculated:

$$\mathring{a}_{\beta 355/532}(R) = -\frac{\log\left[\beta^{\mathrm{par}}_{355}(R)/\beta^{\mathrm{par}}_{532}(R)\right]}{\log(532/355)}, \tag{2.20}$$

$$\mathring{a}_{\beta 355/1064}(R) = -\frac{\log\left[\beta^{\mathrm{par}}_{355}(R)/\beta^{\mathrm{par}}_{1064}(R)\right]}{\log(1064/355)}, \tag{2.21}$$

and

$$\mathring{a}_{\beta 532/1064}(R) = -\frac{\log\left[\beta^{\mathrm{par}}_{532}(R)/\beta^{\mathrm{par}}_{1064}(R)\right]}{\log(1064/532)} \ . \tag{2.22}$$

The extinction-related Ångström exponent can be calculated based on measured pairs of particle extinction coefficients at 355 nm and 532 nm wavelength:

$$\mathring{a}_{\beta 355/532}(R) = -\frac{\log\left[\alpha^{\mathrm{par}}_{355}(R)/\alpha^{\mathrm{par}}_{532}(R)\right]}{\log(532/355)} \ . \tag{2.23}$$

2.2 The PollyXT lidar system

The first Polly, a portable automated two-channel aerosol Raman lidar system Althausen et al. (Polly 2004), was developed at TROPOS in 2003 with the aim to identify vertical profiles of optical properties, aerosol layers in the troposphere and stratosphere, humidity, aerosol type, and aerosol microphysical properties (Althausen et al., 2009; Engelmann et al., 2016). Over the last two decades, the lidar group at TROPOS has continuously improved the instrument and established a network of multiple neXT generation PollyXT systems (Engelmann et al., 2016) called PollyNET (Baars et al., 2016). The lidars are distributed globally with most operating systems in Europe. Therefore supporting European networks like EARLINET (European Aerosol Research Lidar Network)(Pappalardo et al., 2014) as part of ACTRIS (Wandinger et al., 2020; Laj et al., 2024) and Cloudnet (Illingworth et al., 2007) via international collaboration, field campaigns and exchange of knowledge and data (e.g., Hofer et al., 2017; Mamouri et al., 2021). The state-of-the-art PollyXT is a dual-field-of-view multiwavelength polarization Raman lidar, which allows the retrieval of aerosol and cloud microphysical properties. A detailed description of such PollyXT systems is given by Engelmann et al. (2016); Jimenez et al. (2020a) and a technical overview is provided in Fig. 2.1. The lidar in Dushanbe contains a laser that emits light pulses at 1064 nm wavelength, which passes through second and third harmonic generators to simultaneously create additional light pulses at 532 nm and 355 nm wavelength. Since this generation can cause a decrease in purity of the polarization or rotate the polarization plane, a wave-plate and a Brewster-cut Glan-laser polarizer are implemented in the optical path to ensure the purity of the linear polarization of the emitted light. The remaining polarization impurity (fraction of non-linearly polarized light) amounts to less than 0.1 %, which is low enough regarding typical molecular linear depolarization ratios. Before the light is emitted into the atmosphere, a beam expander is used to expand the laser light to 45 mm diameter and reduce the laser divergence to less than 0.2 mrad.

The receiver unit of the used PollyXT consists of a far-range (FR) and near-range (NR) optical set-up. A Newtonian telescope with a 300 mm primary mirror and a field-of-view (FOV) of 1 mrad is used for the far-range measurements. The overlap function of this telescope reaches unity at 800-–900 m (Engelmann et al., 2016). Additionally, the implementation of a NR receiver unit with two separate 50 mm refracting telescopes and FOV's of 2 mrad reduces the overlap-affected height range to 120 m above the lidar, which is favorable for measurements in the planetary boundary layer (PBL) and can be used for data quality insurance and overlap determination for

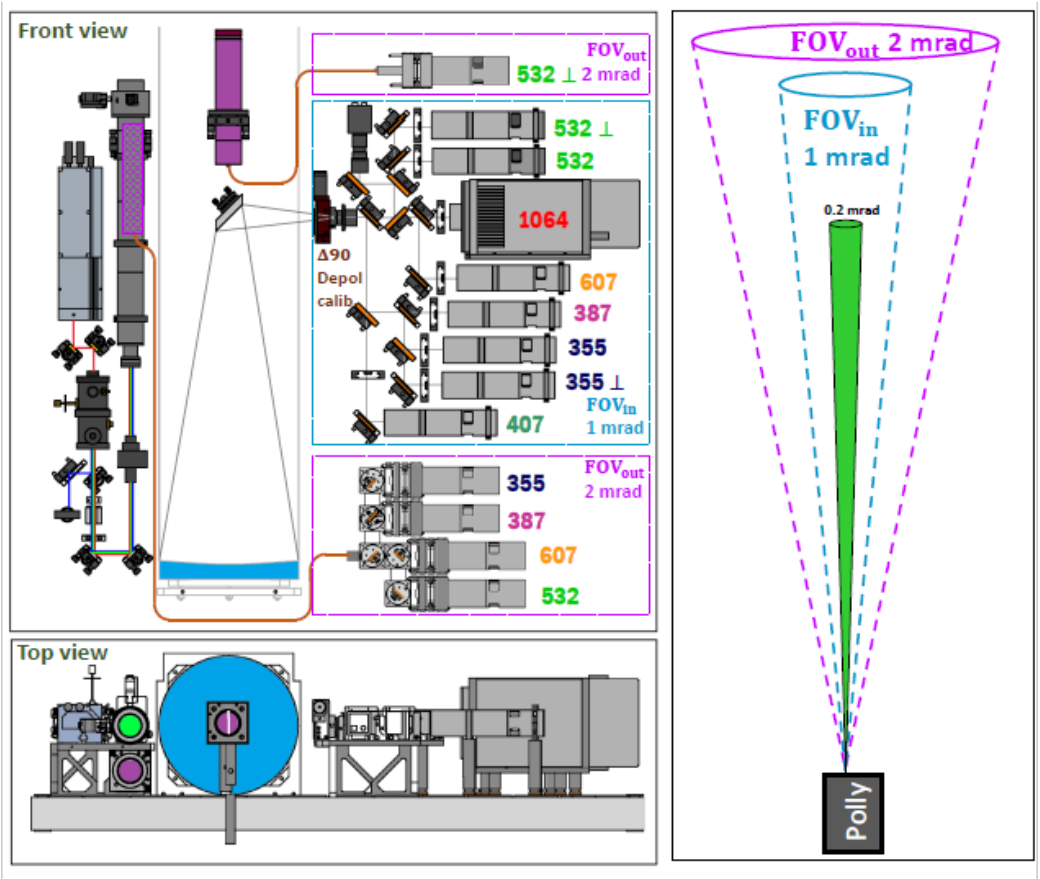

Figure 2.1: The right side of the figure illustrates the dual-FOV polarization lidar geometrical configuration, showing the laser beam and different FOV's with height. On the left the optical setup of the PollyXT lidar (similar to Engelmann et al. (2016)) is shown. The upper left part shows the front view of the system, the lower left part the view from above. Mounted to the left of the main lidar telescope (in blue) is the transmitter unit where the laser light (green circle) is transmitted. As part of the receiver unit the backscattered light is collected with the far-range (FR) telescope (blue circle, FOV = 1 mrad) and then passed to the optical elements and detector channels (enclosed in blue frame for FR receiver). Next to the detector channels are written their wavelengths in nanometers, and ⊥ indicates the cross-polarized channels. For the near-range (NR) receiver unit a 5 cm receiver telescope (purple circle, FOV = 2 mrad) is mounted above the secondary mirror of the FR telescope to collect the cross-polarized signal component. The detector channels of the NR unit are enclosed in the purple frame. Adapted from Jimenez et al. (2020b).

the FR unit. Based on the size of each FOV, the FR unit is the inner FOV and the NR is the outer FOV, which is explained in Sect. 2.4.2. After the telescope, the received light is collimated with optical lenses and spectrally separated into the different wavelengths by dichroic beam splitters. The receiver unit consists of thirteen channels, which measure the backscattered light and partially the cross-polarized and total components of the signal (Jimenez et al., 2020b). The NR channels are at wavelengths of 355 nm, 387 nm, 532 nm, and 607 nm. An additional channel at 532 nm connected to the second telescope of the NR unit is measuring only the cross-polarized light component, which is crucial for the DFOV method described in Sect. 2.4.2. The FR unit consists of channels at wavelengths of 355 nm, 387 nm, 407 nm, 532 nm, 607 nm and 1064 nm as well as two channels for the detection of cross polarized components at 355 nm and 532 nm.
After the detection, every single-shot lidar profile is then transferred to a PC where profiles are averaged to 30 s temporal resolution sampled at 7.5 m vertical resolution.
Since precise measurements of volume and particle depolarization ratio profiles are fundamental for detecting aerosol and cloud microphysical properties, a $\Delta 90°$ calibration (see Sect. 2.1.1) is being performed three times a day (Freudenthaler et al., 2009; Freudenthaler, 2016; Engelmann et al., 2016; Jimenez et al., 2020b). For this purpose, a remote-controlled rotatable sheet polarizer is mounted at the FR receiver in front of the pinhole. In order to retrieve the absolute calibration constant V^*, which is given in Eq. 2.18, the polarizer is rotated automatically by $-45°$ and $+45°$ with respect to the laser polarization plane in the light path for calibration to determine ${}^{-45°}\delta'(R)$ and ${}^{+45°}\delta'(R)$. Because of signal noise and varying atmospheric conditions during calibration measurements, the resulting profiles of V^* vary with height. Therefore, cloud-free, clear-sky conditions are most favorable for the measurement of V^*. Additionally, profiles are vertically averaged over several kilometers to reduce the impact of signal noise on V^*. Based on the assumption that the depolarization ratios for $\mathrm{FOV_{in}}$ and $\mathrm{FOV_{out}}$ are equal when cloud-free, clear-sky conditions are given, the calibration constant for the NR ($\mathrm{FOV_{out}}$) is also derived. Both, V^*_{out} and V^*_{out} are used for the calculation of the inner and outer FOV volume depolarization ratio.

2.3 PollyNET Processing Chain

The PollyNET processing chain is described in the following section based on Baars et al. (2016). The automatized processing chain provides the aerosol information, while the cloud products were computed automatically with an external module.

The continuous observations with PollyNET lidars are screened for appropriate weather conditions and processed in near-real time. Profiles of the particle backscatter coefficient (355, 532, and 1064 nm), the particle extinction coefficient (355 and 532 nm), the particle depolarization ratio (355 and 532 nm) and water vapor mixing ratio are retrieved in an automatic framework. An overview of the retrieved parameters and further relevant information are available on the webpage of PollyNET (link: polly.tropos.de). In detail, the processing chain monitors and discards measurement periods which are affected by inappropriate weather conditions like fog. Several corrections are performed on the preprocessing stage, such as deadtime, background and range correction. Additionally, to improve near-range capabilities, an overlap correction can be applied (Wandinger and Ansmann, 2002). To avoid erroneous retrievals due to incomplete overlap, for example caused by small temperature fluctuations, the lowermost height bins are discarded. Afterwards, cloud screening is performed based on range- and background-corrected signals following Baars et al. (2008). After the whole measurement period has been analyzed and screened for clouds, the preprocessing algorithm looks for as many 30 min intervals as possible that are fully cloud-free in the lowest 9 km. The range- and background-corrected lidar signals in the selected 30–90 min intervals are averaged and are used as input for finding the reference height. The search for the cloud-free signals is not fixed to specific times and only based on finding a clear-sky time period. The 30 min averaging of lidar signals increases the signal-to-noise-ratio (SNR).

In order to find the optimal reference height interval, a Rayleigh fit (e.g., Freudenthaler et al., 2018) is performed for as many height intervals, for which the total SNR is greater than a wavelength-dependent threshold. After several tests, the reference height interval with the best results is selected. Lastly, the aerosol classification algorithm, based on retrieved optical properties like Ångström exponent and depolarization ratio which are influenced by size and shape of the particles, is implemented.

2.3.1 High-temporal-resolution products

In order to achieve high-temporal-resolution products, which have been referred to as quasi-products in earlier studies (e.g., Baars et al., 2017; Jimenez, 2021), the lidar signal is calibrated with a lidar calibration constant as described by Jimenez (2021). This constant is calculated based on high-quality backscatter and extinction profiles obtained during cloud-free conditions. The lidar system parameter C_λ, also called lidar constant, can be computed as:

$$C_\lambda(R) = \frac{P(R,\lambda)R^2}{\left[\beta_\lambda^{\mathrm{par}}(R) + \beta_\lambda^{\mathrm{mol}}(R)\right] O_\lambda(R)} \cdot \exp\left\{2\int_0^R \left[\alpha_\lambda^{\mathrm{par}}(r) + \alpha_\lambda^{\mathrm{mol}}(r)\right] \mathrm{d}r\right\} . \tag{2.24}$$

This parameter is used to calculate the attenuated backscatter coefficient $\beta_\lambda^{\mathrm{att}}$ as follows

$$\beta_\lambda^{\mathrm{att}} = \frac{P(R,\lambda)R^2}{C_\lambda O_\lambda(R)} = \left[\beta_\lambda^{\mathrm{par}}(R) + \beta_\lambda^{\mathrm{mol}}(R)\right] T_\lambda^{\mathrm{par}}(R)\, T_\lambda^{\mathrm{mol}}(R) , \tag{2.25}$$

where $T_\lambda^{\mathrm{par}}(R)$ and $T_\lambda^{\mathrm{mol}}(R)$ represent the transmission through aerosol particles and molecules.
The attenuated backscatter is a very practical quantity as it contains only information about the optical atmospheric situation, from which the backscatter coefficient can be constructed. Because, initially, the particle backscatter over the whole atmosphere, and therefore T^{par}, is unknown. The backscatter coefficient can be computed in an iterative manner starting with a transmission value $T^{\mathrm{par}} = 1$ as a first guess. The initial particle backscatter $\beta_{\lambda*}^{\mathrm{par}}(R)$ is calculated as:

$$\beta_{\lambda*}^{\mathrm{par}}(R) = \frac{\beta_\lambda^{\mathrm{att}}(R)}{T_\lambda^{\mathrm{mol}}(R)} - \beta_\lambda^{\mathrm{mol}}(R) . \tag{2.26}$$

Then, by assuming a value of S_λ^{par}, a first guess of the particle extinction coefficient $\alpha_\lambda^{\mathrm{par}}(R)$ can be calculated as:

$$\alpha_\lambda^{\mathrm{par}}(R) = S_\lambda^{\mathrm{par}}(R) \cdot \beta_\lambda^{\mathrm{par}}(R) . \tag{2.27}$$

Afterwards, the high resolution extinction coefficient is used to calculate the transmission through aerosol particles $T_{\lambda*}^{\mathrm{par}}(R)$ by

$$T_{\lambda*}^{\mathrm{par}}(R) = \exp\left[-2\int_0^R \alpha_{\lambda*}^{\mathrm{par}} \mathrm{d}r\right] . \tag{2.28}$$

Finally, the high resolution aerosol backscatter coefficient ${}^{\mathrm{HR}}\beta_{\lambda}^{\mathrm{par}}(R)$ can be retrieved:

$$ {}^{\mathrm{HR}}\beta_{\lambda}^{\mathrm{par}}(R) = \frac{\beta_{\lambda}^{\mathrm{att}}(R)}{T_{\lambda}^{\mathrm{mol}}(R)\, T_{\lambda*}^{\mathrm{par}}(R)} - \beta_{\lambda}^{\mathrm{mol}}(R) \ , \tag{2.29} $$

which subsequently allows the retrieval of further high resolved optical properties like the particle depolarization ratio at 355 and 532 nm.
The obtained high resolution products have a temporal resolution of 30 s and a vertical resolution of 30 m and are obtained for each 6 h measurement period. Such high resolution parameters improve the detection of atmospheric aerosol layers and enable the investigation of aerosol-cloud-interactions as presented in this study.

2.4 Aerosol particle, cloud and air mass characterization

The objective of this study is to combine the outcomes from two different methods, namely the The Polarization Lidar Photometer Networking method (POLIPHON) and the Dual-Field-of-View (DFOV) method. By utilizing POLIPHON, comprehensive details about the properties of aerosols can be obtained. Additionally, the DFOV-method enables the retrieval of cloud microphysical properties from cloud base up to 75 m into the cloud.
The combined approach is expected to provide a more complete understanding of atmospheric microphysical processes by integrating the knowledge acquired from both methods. This allows a comprehensive analysis of the interaction between aerosols and clouds, as well as their impact on the climate.

2.4.1 Retrieval of microphysical and cloud-relevant properties

The Polarization Lidar Photometer Networking method (POLIPHON Mamouri and Ansmann, 2016; Ansmann et al., 2019) utilizes the particle backscatter coefficient and the particle linear depolarization ratio profiles at 532 nm wavelength to first separate dust and non-dust particle backscatter coefficients (Mamouri and Ansmann, 2016). The method is based on typical particle linear depolarization ratios for dust ($\delta_{\mathrm{d}} = 0.31$) and non-dust

($\delta_{\mathrm{nd}} = 0.05$) (Müller et al., 2007; Tesche et al., 2009). The calculations of the dust β_{d} and non-dust particle backscatter coefficient β_{nd} are as follows:

$$\beta_{\mathrm{d}} = \beta^{\mathrm{par}} \frac{(\delta^{\mathrm{par}} - \delta_{\mathrm{nd}})(1 + \delta_{\mathrm{d}})}{(\delta^{\mathrm{par}} - \delta_{\mathrm{nd}})(1 + \delta^{\mathrm{par}})} \tag{2.30}$$

and

$$\beta_{\mathrm{nd}} = \beta_{\mathrm{par}} - \beta_{\mathrm{d}} \ . \tag{2.31}$$

The separation is applicable for particle depolarization ratios $\delta_{\mathrm{nd}} \leq \delta^{\mathrm{par}} \leq \delta_{\mathrm{d}}$. $\beta_{\mathrm{nd}} = \beta^{\mathrm{par}}$ is set for $\delta^{\mathrm{par}} \leq \delta_{nd}$ and $\beta_{\mathrm{d}} = \beta^{\mathrm{par}}$ for $\delta^{\mathrm{par}} \geq \delta_{\mathrm{d}}$, respectively. Afterwards, these dust and non-dust backscatter coefficient profiles along with typical lidar ratio values for dust ($S_{\mathrm{d}} = 40\,sr$, (Hofer, 2020)) and non-dust ($S_{\mathrm{nd}} = 50\,sr$, (Hofer, 2020)) are used to calculate dust and non-dust particle extinction coefficient profiles as follows:

$$\alpha_{\mathrm{d}} = \beta_{\mathrm{d}} \cdot S_{\mathrm{d}}^{\mathrm{par}} \tag{2.32}$$

and

$$\alpha_{\mathrm{nd}} = \beta_{\mathrm{nd}} \cdot S_{\mathrm{nd}}^{\mathrm{par}} . \tag{2.33}$$

Then, conversion factors and generic densities of dust and non-dust are used to convert the extinction profiles to number concentration profiles as

$$n_{100,\mathrm{d}} = C_{\mathrm{n100,d}} \cdot \alpha_{\mathrm{d}}^{\mathrm{b_d}} \ , \tag{2.34}$$

with the exponent for dust $b_{\mathrm{d}} = 0.71$ and the conversion factor $C_{\mathrm{n100,d}} = 12.4\,\mathrm{Mm\,cm^{-3}}$ and

$$n_{50,\mathrm{nd}} = C_{\mathrm{n60,nd}} \cdot \alpha_{\mathrm{nd}}^{\mathrm{b_{nd}}} \tag{2.35}$$

with the exponent for non-dust $b_{\mathrm{nd}} = 0.94$ and the conversion factor $C_{\mathrm{n60,nd}} = 25.7\,\mathrm{Mm\,cm^{-3}}$ (Ansmann et al., 2019; Hofer, 2020). For pollution-related estimations of CCN concentrations, a dry activation radius of 50 nm is assumed. However, accounting for typical moisture conditions which can cause hygroscopic haze aerosol particles to grow, the conversion factor $C_{\mathrm{n60,nd}}$ assumes that these particles of radii > 60 nm are representing dry haze aerosol particles that have dry radii of > 50 nm (Hofer, 2020). These conversion factors originate from long-term AERONET (Aerosol Robotic Network, Holben et al. (1998, 2001)) measurements of aerosol optical thickness (AOT) and retrieved particle number concentrations (Dubovik and King, 2000; Dubovik et al., 2006) in Dushanbe (Ansmann et al., 2019). The threshold for dust ($\mathring{a} < 0.3$, AOT > 0.1) and non-dust ($\mathring{a} > 1.4$) scenarios was applied to the Ångström exponent ($\mathring{a}$) from the 440–880 nm spectral range and AOT at 500 nm (Mamouri and Ansmann, 2016; Ansmann et al., 2019). In the

case of dust, the conversion links the extinction coefficient to the number concentration of particles with a radius larger than 100 nm :

$$n_{\mathrm{CCN,d}} = f_{\mathrm{e,d}} \cdot n_{100,\mathrm{d}} \ , \tag{2.36}$$

with the enhancement factor for dust $f_{\mathrm{e,d}} = 1$.
For the estimation of non-dust CCN concentrations profiles of number concentration of non-dust particles with a radius larger than 50 nm ($n_{50,\mathrm{nd}}$) are used (Ansmann et al., 2019; Lv et al., 2018):

$$n_{\mathrm{CCN,nd}} = f_{\mathrm{e,nd}} \cdot n_{50,\mathrm{nd}} \ , \tag{2.37}$$

with the enhancement factor for non-dust $f_{\mathrm{e,nd}} = 1$. Both enhancement factors are dependent on supersaturation. These CCN concentration estimates are based on the assumption of typical water supersaturation of 0.2 % (Siebert and Shaw, 2017). Since this study only involves liquid water clouds, the retrieval procedure for INP-relevant properties is not included but can be found in e.g., Hofer et al. (2020a) .

2.4.2 Dual-Field-of-View depolarization method

The Dual-Field-of-View polarization method expands the lidar measurements to observe liquid water cloud properties. This method is based on multiple scattering (MS), which is related to optical and microphysical properties of cloud droplets and is described by Jimenez (2021).
In dense liquid water clouds, one or more forward scattering events occur. Forward scattering changes dependent on the size of the cloud droplet. For smaller droplets, the forward scattering will be spread wider as for larger droplets, where forward scattering will take place with a much narrower forward scattering lobe. This can be seen in the phase function of two droplets of different sizes. This is shown in Fig. 2.2 on the left, where the phase function for droplets with effective radii of 3 µm, 8 µm, 13 µm and 18 µm are displayed. Especially in the forward scattering regime, differences between small and large droplets can be observed, which represents a dependency of the scattering angle with droplet sizes. In the backscattering region, these size-related features might be out smoothed, but in the depolarization ratio, the size information remains.
If the lidar detects photons, backward scattering had to take place, but if first forward scattering took place and then backward scattering, the scattering angle at which the photons are scattered back to the lidar is close

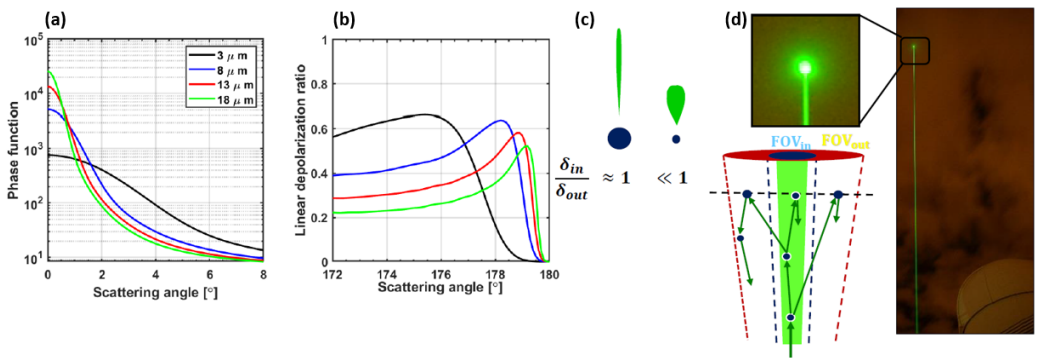

Figure 2.2: (a) Phase function versus scattering angle for different droplet sizes. (b) Linear depolarization ratio versus scattering angle for different droplet sizes. (c) Illustration of size dependency between the droplet size and the elongation of the phase function in the near-forward direction. (d) Illustration of multiple scattering (MS) events with a picture of the MS effect of the laser beam at a cloud layer. Adapted from Jimenez (2021).

to 180° but different from it.
Usually, cloud droplets during single scattering events do not change the polarization of light due to their spherical shape if the light is backscattered at 180°. But if multiple scattering occurs and the final backscatter angle is close to 180° but different from it, the depolarization increases strongly. This also changes for different effective radii of cloud droplets, because for smaller droplets, the forward scattering will be spread wider as for larger droplets with a more narrow forward scattering lobe, which is shown in Fig. 2.2 for two droplets with their respective forward scattering of the laser beam. This size dependency also influences the linear depolarization ratio between the inner and outer FOV shown in Fig. 2.2. Measuring depolarization at two different FOV's, one inner and one outer FOV, allows to retrieve cloud properties due to the dependency of the polarization state on the size of the cloud droplets.
Based on these size dependencies, due to multiple scattering (MS), liquid water cloud properties in high temporal resolution of 30–120 s can be derived from day and nighttime observations.
This relationship between size of cloud droplets and depolarization can be used to finally derive the cloud properties effective radius, cloud extinction coefficient, liquid water content, and cloud droplet number concentration. For this retrieval, a MS model is used to simulate polarization lidar measurements for various different parameters (Jimenez et al., 2020a). Vertical profiles of the cloud properties are computed for a penetration height into

the cloud of 75 m above cloud base (z_{ref}). The calculated vertical profiles of the cloud properties are used to simulate cross- and co-polarized lidar backscatter coefficients, which subsequently return volume depolarization ratios. The performed simulations are based on the assumption of subadiabatic conditions regarding constant cloud droplet number concentration and linearly increasing liquid-water content, because of computational limits of the MS model regarding time and costs. The overall concept is illustrated in Fig. 2.3. The computations are made for two FOV's and 720 different cloud

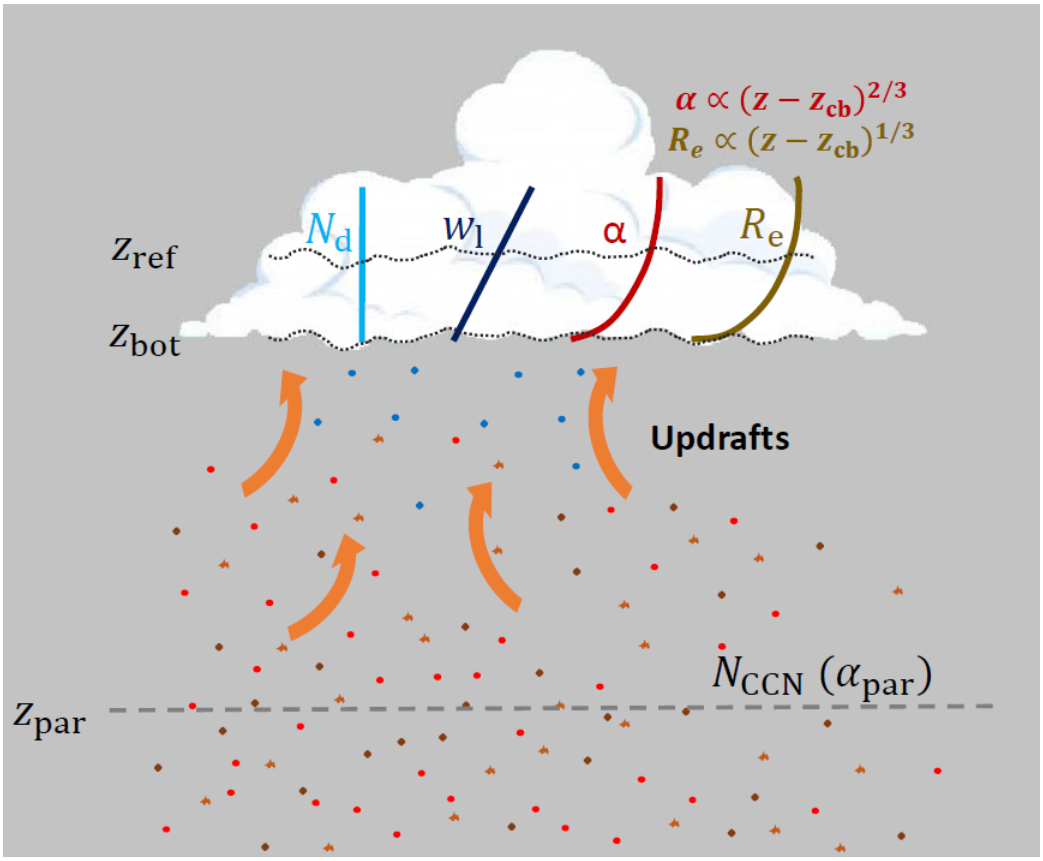

Figure 2.3: Illustration of the overall concept to investigate clouds and aerosol-cloud interactions. Assumptions and parameterizations are subadiabatic conditions in the lowest part of the cloud layer, a height-independent droplet number concentration, and a linearly increasing liquid-water content. The cloud extinction coefficient and droplet effective radius profiles are calculated. Adapted from Jimenez (2021).

scenarios with a cloud depth of 200 m and a vertical resolution of 7.5 m. The inner field-of-view $\mathrm{FOV_{in}}$ is 1 mrad and the outer field-of-view $\mathrm{FOV_{out}}$

is 2 mrad, based on sensitivity towards droplet effective radius and cloud inhomogeneities. Combining the modelled relationship between effective radius and depolarization ratio of $\mathrm{FOV_{in}}$ and $\mathrm{FOV_{out}}$ for different scenarios, which has a low dependency on the cloud extinction coefficient, with actual measured ratios of $\mathrm{FOV_{in}}$ and $\mathrm{FOV_{out}}$ depolarization allows the retrieval of the effective radius, which is calculated as follows:

$$R_{\mathrm{eff}}(z_{\mathrm{ref}} = 75\,\mathrm{m}) = B_0 + B_1 \times \bar{\delta}_{\mathrm{rat}} + B_2 \times \bar{\delta}^2_{\mathrm{rat}} + B_3 \times \bar{\delta}^3_{\mathrm{rat}}\ , \tag{2.38}$$

with the polynomial coefficients R_0, R_1, R_2, and R_3 (Jimenez et al., 2020a) and the DFOV ratio of depolarization ratios $\bar{\delta}_{\mathrm{rat}}$, which can be described as:

$$\bar{\delta}_{\mathrm{rat}}(z_{\mathrm{bot}}, z_{\mathrm{ref}}) = \frac{\bar{\delta}_{\mathrm{in}}(z_{\mathrm{bot}}, z_{\mathrm{ref}})}{\bar{\delta}_{\mathrm{out}}(z_{\mathrm{bot}}, z_{\mathrm{ref}})}\ . \tag{2.39}$$

Here, z_{bot} represents the height of the cloud base. Using the obtained effective radius and the inner FOV depolarization ratio allows the retrieval of the cloud extinction coefficient which is calculated with:

$$\alpha_{\mathrm{c}}(z_{\mathrm{ref}} = 75\,\mathrm{m}) = \alpha_0(R_{\mathrm{eff}}, z_{\mathrm{bot}}) + \alpha_1(R_{\mathrm{eff}}, z_{\mathrm{bot}}) \times \bar{\delta}_{\mathrm{in}} + \alpha_2(R_{\mathrm{eff}}, z_{\mathrm{bot}}) \times \bar{\delta}^2_{\mathrm{in}}\ . \tag{2.40}$$

Based on the effective radius and the cloud extinction coefficient, the liquid water content LWC can be derived from:

$$LWC = \frac{2}{3}\rho_w \alpha_{\mathrm{c}} R_{\mathrm{eff}}, \tag{2.41}$$

and the cloud droplet number concentration can be calculated with

$$N_{\mathrm{d}} = \frac{1}{2\pi\kappa}\alpha_{\mathrm{c}} R_{\mathrm{eff}}^{-2}, \tag{2.42}$$

with κ describing the ratio between the volume mean droplet radius R_{v} and the effective radius R_{eff} based on in situ measurements in warm stratified clouds by Martin et al. (1994):

$$\kappa = \frac{R_{\mathrm{v}}^3}{R_{\mathrm{eff}}^3} = 0.75\ . \tag{2.43}$$

The described retrieval is shown exemplary in Fig. 2.4. On the left side of Fig. 2.4, the known relationship between the linear depolarization ratio of the $\mathrm{FOV_{in}}$ and $\mathrm{FOV_{out}}$ with the effective radius of the cloud droplet is represented

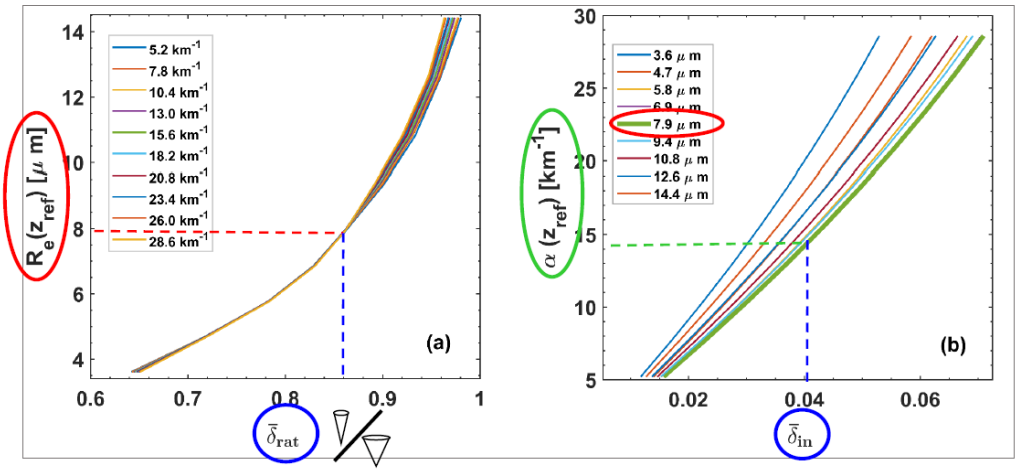

Figure 2.4: Example for two-step approach to retrieve effective radius and cloud extinction coefficient. (a) The droplet effective radius (circled in red) versus the measured ratio of the linear depolarization ratios of the FOV_{in} and FOV_{out} (circled in blue) for different cloud extinction coefficients. The exemplary ratio of the linear depolarization ratio of the FOV_{in} and FOV_{out}, is indicated with the blue dotted line. The red dotted line then show the retrieval of the droplet effective radius, which is here 7.9 µm. The next step of the retrieval is shown on the right. (b) Here the cloud extinction coefficient versus the measured FOV_{in} depolarization ratio for different effective radii is shown. The exemplary FOV_{in} depolarization ratio is indicated with the blue dotted line. Based on this and the previous obtained effective radius of 7.9 µm, the cloud extinction coefficient can be retrieved, indicated by the red dotted line. Adapted from Jimenez et al. (2020a).

for different cloud extinction coefficients, which has a low dependency on the linear depolarization ratio. The linear depolarization ratio of the FOV_{in} and FOV_{out}, which is marked with a blue circle, is measured and used to derive the effective radius, indicated with the dotted lines. In this example, an effective radius of 7.9 µm is obtained. The next step makes use of the measured FOV_{in} depolarization and calculated cloud extinction coefficients for different effective radii, which show a clear dependency of the cloud extinction coefficient on the effective radius and the depolarization ratio of the FOV_{in}. Since the effective radius as well as the FOV_{in} depolarization are known, the cloud extinction coefficient can be retrieved, indicated by the dotted lines. Based on both cloud properties, the liquid water content as described in Eq. 2.41 and the cloud droplet number concentration as described in Eq. 2.42 can be calculated.

The technical implementation of the DFOV technique into PollyXT is shown in Fig. 2.1. The channels for the FOV_{in} are marked with the blue box and for the FOV_{out}, with a purple box. For the realization of the DFOV method, a new cross-polarized channel at 532 nm and a lens-telescope with a polarizer on top to ensure angular adjustments of the polarizer and to measure the cross-polarized light were built into PollyXT. Otherwise, the systematic and optical set-up is the same and can be found in detail in Engelmann et al. (2016).

2.4.3 Analysis scheme

This section describes in detail the data processing that was performed for this thesis. The base data set comes from high-resolution measurements from the DFOV Raman polarization lidar PollyXT stationed in Dushanbe, Tajikistan (38° 33′ 34″ N, 68° 51′ 22″ E) at an altitude of 864 m a.s.l. This data baseline, which covers the period from June 2019 to July 2023 with interruptions due to repairs, provides the foundation for this aerosol-cloud study.
The DFOV dataset comes as time series of the cloud parameters, such as cloud base (CB), cloud extinction coefficient α_c, liquid water content LWC and cloud droplet number concentrations N_d with their respective uncertainties. They have a temporal resolution of 3 minutes. The PollyNET optical products come as averaged profiles during cloud free periods, and as high-temporal-resolution profiles, based on calibration constants (see Sect. 2.3.1). The high-resolution products are still under development, and during this study, efforts were put into these products to extend the coverage of the analysis, covering scales from some minutes to seasonal scale.
To study the long-term observations, the averaged profiles were considered, while for short-term cases, the high-resolution products were considered only. With regard to the aerosol, the particle backscatter coefficient is the primary operational product provided by the PollyNET automatic processing chain. There are two product versions available: high quality profiles from averaged cloud-free periods in which a Rayleigh fit in the free troposphere is possible (Baars et al., 2016), and high-temporal-resolution products that cover even cloudy periods (see Sect. 2.3.1). Both versions are considered in this study. The averaged profiles provide the most accurate information about the aerosol situation and were used to study the aerosol-cloud relation in the long-term. However, this version cannot be used to look into the cloud properties below an evolving cloud. For single cloud cases, the high-resolution products were used. The automatic retrieval is performed in a 6 h frame and depends on the calibration constant derived from the high-quality cloud-free backscatter coefficient profiles within the 6 h - period. The product is still a

task under development, and discontinuities were present when looking at longer periods. For this work, local runs of the PollyNET automatic processing chain were performed to provide this product. For the selected cloud cases, the lidar calibration constants needed for the high-temporal-resolution products were set as the average of the constants from all cloud-free profiles close to the scene.

From the whole data set, single individual clouds were identified and indexed. To identify cloud scenes, a time gap of 1 h was set as criterion to separate individual clouds. So if the previous cloud time bin was longer than an hour ago, a new cloud was counted. Overall, based on the one hour break in between clouds, 1602 liquid water clouds were detected during the 28 months of measurements.

For the entire data set, the information associated to the cloud scenes detected was extracted, and the POLIPHON method was applied using the particle backscatter coefficient and particle depolarization ratio at 532 nm wavelength. Then for each profile the set of POLIPHON products, namely the dust and non-dust backscatter coefficients, and the CCN number concentrations of dust and non-dust, were computed.

For the short-term study, the POLIPHON method was applied to the averaged particle backscatter coefficient profiles and particle depolarization ratio profiles of the two days before and the two days after the cloud event to obtain temporal averages of vertical profiles of those properties.

To look into single cases in detail, the high-temporal-resolution products were the input for the POLIPHON method.

For the long-term analysis, collocated data sets were generated from the aerosol and cloud properties. For each single cloud, the properties were averaged to obtain one mean value per cloud. Then, the corresponding profiles of CCN number concentrations N_{CCN}, which were calculated from all available backscatter coefficient and depolarization ratio profiles, were averaged temporally for the time range between two days before the cloud event and two days after the cloud event. Then, these mean N_{CCN} profiles were vertically averaged between 500 m above ground and 300 m below cloud base to retrieve mean CCN concentration values. The measurements from 500 m above the lidar were selected to obtain sufficient overlap between laser beam and telescope (Jimenez et al., 2020b). The first 300 m below CB were discarded to exclude aerosol particles that are potentially influenced by hygroscopicity effects, because directly below the cloud, the moisture is higher, which causes growth of the aerosol particles causing invalid retrievals of CCN number concentrations (Jimenez et al., 2020b).

Updraft velocity is the other important parameter in the aerosol-cloud relation. Because no measurements of this quantity are available, as indi-

cation and to consider the influence of the meteorological situation, the Brunt-Väisälä frequency was calculated to obtain information about the atmospheric stability. It was calculated based on meteorological data from GDAS (Global Data Assimilation System) (GDAS, 2024) (for the location 39° N,68° E). The same GDAS data was used for pressure and temperature input in the PollyNET retrieval of the aerosol products.
The Brunt-Väisälä frequency is the frequency of an oscillating air parcel in a stable atmosphere. A positive value of the Brunt-Väisälä-frequency indicates stable atmospheric conditions, a value close to zero indicates neutral stability and negative values represent rather unstable atmospheric conditions. The Brunt-Väisälä-frequency is calculated as follows (Stull, 2017):

$$N^2 = \frac{g}{\Theta_v} \cdot \frac{\delta \Theta_v}{\delta \mathrm{z}} \ , \tag{2.44}$$

with the potential temperature Θ :

$$\Theta = T \left(\frac{p_0}{p} \right)^{\frac{R}{c_p}} \ , \tag{2.45}$$

with the specific gas constant $R = 287.05 \, \frac{\mathrm{J}}{\mathrm{kg\ K}}$, the specific heat capacity for a constant pressure $c_\mathrm{p} = 1004 \, \frac{\mathrm{J}}{\mathrm{kg\ K}}$, the standard pressure at ground level $p_0 = 1000 \, \mathrm{hPa}$ and the virtual potential temperature Θ_v:

$$\Theta_v = \Theta \cdot (1 + 0.61 \cdot WVMR) \ , \tag{2.46}$$

with the water vapor mixing ratio $WVMR$ being:

$$WVMR = RH \cdot \omega_s \ , \tag{2.47}$$

with RH is the relative humidity and the water vapor mass mixing ratio:

$$\omega_s = 0.622 \cdot \frac{E_s}{p - E_s} \tag{2.48}$$

and the saturation vapor pressure:

$$E_s = 6.107 \, \mathrm{hPa} \cdot \exp \left\{ \frac{17.3 \cdot \tau}{238 + \tau} \right\} \ , \tag{2.49}$$

where τ represents the temperature in degree Celcius.
The temperature gradient ∇T was calculated using the difference in temperature of the GDAS data. In the calculation, Δz represents the difference in altitude between data points, with each point corresponding to an altitude

range of 100 meters:

$$\nabla T = \frac{\Delta T}{\Delta z} \ . \tag{2.50}$$

And based on Choudhury and Tesche (2022a), the r_{wet} and r_{40} were calculated to be applied to the relative humidity (RH) from the GDAS data. Subsequently, they were used to correct all N_{CNN} values, because in moist conditions, hygroscopic aerosol particles can grow, which needs to be accounted for before retrieving N_{CNN} from optical quantities that are related to size. The hygroscopoicity correction can be expressed as (Choudhury and Tesche, 2022a):

$$\frac{r_{\text{wet}}(RH)}{r_{40}} = \left(1 + \kappa \cdot \frac{RH}{100 - RH}\right)^{\frac{1}{3}} \ , \tag{2.51}$$

with κ chosen as 0.4. For the dry factor r_{40}, in the region of Tajikistan, a RH of 40 % was chosen.
The hygroscopicity corrected CCN number concentration $N_{\text{CCN,corr}}$ is retrieved with:

$$N_{\text{CCN,corr}} = \frac{r_{\text{wet}}(RH)}{r_{40}} \ . \tag{2.52}$$

2.4.4 Aerosols and clouds in Tajikistan

In earlier studies with lidar measurements in Tajikistan from Hofer (2020); Jimenez (2021); Engelmann et al. (2019), aerosol properties and cloud microphysical properties have been investigated during short time periods of 8 (Jimenez, 2021) to 16 months (Hofer, 2020). First, the lidar measurements obtained during the CADEX (Central Asian Dust Experiment, Hofer et al. (2017)) campaign resulted that the aerosol composition in Dushanbe varied vertically and temporally, with complex mixtures of pollution and dust. High depolarization ratios which indicate polluted dust aerosol were measured while simultaneously showing low lidar ratios which potentially indicate salty dust. This can be explained by lakes in Central Asia which have dried out like the Aral Sea, and left behind fine sand that has higher contributions of evaporates and can be easily lifted up into the atmosphere and transported long distances (Abuduwaili et al., 2010). Such salty dust has been observed at different measurements sites in Central Asia, (e.g., Hofer, 2020; Abuduwaili et al., 2010; Singer et al., 2003) and transport trajectories have shown that air masses reach Dushanbe from north west (Uzbekistan) crossing the Aralkum, from Afghanistan (south west), from

the Arabian Peninsula, and from local emissions (Lipken et al., 2024). Such salty aerosol mixtures could affect the solubility of aerosols and therefore make them more favorable for CCN activation.
Still, Tajikistan has a dry-continental climate, affected by dust which is more likely to work as an ice-nucleating particle, supporting the formation of ice-containing mixed-phase clouds at high altitudes (Hofer, 2020). Jimenez (2021) has additionally investigated cloud properties based on only 8 months of measurements. During this period, the observations showed that in Dushanbe many CCN particles were not activated, based on the low value of droplet number concentrations compared to the CCN number concentration estimates. The suggested explanations for such observations are that Tajikistan represents an updraft-limited regime. An updraft-limited regime is characterized by low updraft strength, a water-vapor supersaturation of usually less than 0.2 %, and the ACI index may be as low as 0.2 – 0.5 (Reutter et al., 2009; Huang et al., 2022). Conversely, in an aerosol-limited regime, updrafts are strong, water-vapor supersaturation typically exceeds 0.5 %, and therefore, the ACI index is high (close to 1)(Reutter et al., 2009; Jimenez, 2021; Huang et al., 2022). Another explanation or influence is the available moisture, which is limited in Tajikistan. Currently, the CCN concentrations estimated with the POLIPHON method (Mamouri and Ansmann, 2016; Tesche et al., 2009) are based on the assumption of a supersaturation of 0.2 % for the activation of the CCN particle. When less droplets are activated than N_{d} are present, this indicates that a supersaturation of 0.2 % was potentially not reached. Warm clouds, which cover about one-third of the Earth's surface, constitute roughly half of all cloud formations globally (Lohmann et al., 2016). These clouds primarily develop in the planetary boundary layer (PBL) and play a significant role in aerosol radiative forcing through aerosol-cloud interactions (ACI) (Heyn et al., 2017). Low-altitude clouds reflect a significant portion of incoming solar radiation, exerting a cooling influence on the Earth's surface. In contrast, high, semi-transparent clouds contribute to warming by trapping outgoing thermal radiation (Rosenfeld et al., 2014). The effect on warm clouds largely stems from variations in droplet number concentration. In regions with high levels of cloud condensation nuclei (CCN), typically polluted areas, clouds exhibit more numerous and smaller droplets compared to those in cleaner environments with identical water content. This increase in droplet surface area and optical thickness enhances the cloud's albedo, making them more reflective and reducing the solar radiation that reaches the Earth's surface, a phenomenon known as the Twomey effect (Twomey, 1959, 1977). Satellite observations estimate that this effect contributes approximately $-1.1\,\mathrm{W/m^2}$ to global anthropogenic radiative forcing (Hasekamp et al.,

2019). The magnitude of this radiative forcing is dependent on the number of aerosol particles acting as CCN and their activation properties. Under dry atmospheric conditions above the PBL, increased cooling at the cloud tops and enhanced cloud-top entrainment in polluted clouds accelerate the evaporation of cloud droplets, reducing the liquid water content in polluted clouds relative to their clean counterparts (Ackerman et al., 2004). This interplay of processes highlights the complex mechanisms that influence cloud microphysical properties.
In order to quantify aerosol and liquid water-cloud interactions, the efficiency or aerosol-cloud-interaction index $E_{\mathrm{aci}}^{N_{\mathrm{d}}}$ can be calculated based on the CCN number concentration N_{CCN} and droplet number concentration N_{d} (Jimenez, 2021):

$$\mathrm{E}_{aci}^{N_d} = \frac{\partial_{\ln} N_{\mathrm{d}}}{\partial_{\ln} N_{\mathrm{CCN}}} \ . \tag{2.53}$$

Since aerosols and clouds act on various temporal scales, it is important to examine the index on different scales (Jimenez, 2021). Therefore, when evaluating the ACI index, the choice of temporal scales, such as short-term, monthly, or seasonal, is crucial since it significantly influences the interpretation and results of the index (Jimenez, 2021; McComiskey and Feingold, 2012).

2.4.5 Time-height resolved air mass source attribution tool

As an additional source of information on the air masses in Dushanbe and therefore the aerosol conditions, the air mass source attribution tool described by Radenz et al. (2021b) was prepared for the application to the region of Dushanbe, Tajikistan, by selecting distinct source regions influencing Dushanbe (Lipken et al., 2024).
The spatial and temporal resolved air mass source attribution scheme utilizes automated backward trajectory calculations and geographical information, which are based on a land cover classification mask and manually defined geographical areas. For the computation of the transport pathway of an air mass arriving over Dushanbe, either mean-wind trajectories using the HYSPLIT (HYbrid Single-Particle Lagrangeian Integrated Trajectory) Model (Stein et al., 2015) or the particle dispersion model FLEXPART (FLEXible PARTicle dispersion model) (Stohl et al., 2005; Pisso et al., 2019) can be used. For the former, meteorological input data from the Global Data Assimilation System data set at 1° horizontal resolution (GDAS) from the

Air Resources Laboratory (ARL) of the U.S. National Weather Service's National Centers for Environmental Prediction (NCEP) is used and the location of the air parcel is stored in 1 h steps. For the latter, meteorological data are obtained from the GFS (Global Forecast System) analysis at a horizontal resolution of 1°. Here, for each height level, 500 particle releases are used, with the particle positions being stored every 3 h. For this study, FLEXPART backward trajectories were used.

Figure 2.5: View from space (height 10908 km) of map of seven geographical regions *Central Asia*, *North East Asia*, *Europe*, *Persia*, *Arabian Peninsula*, *India* and *Sahara* selected for the air mass source attribution for Dushanbe, Tajikistan (marked with red star) (Lipken et al., 2024). Made with Google Earth (Data SIO, NOAA, U.S. Navy, NGA, GEBCO, Image Landsat / Copernicus, Image IBCAO).

The properties of an air parcel arriving over a location of interest are characterized by a certain surface type if the air was close to the surface during its traveled path. The proximity to the surface can be parameterized as a reception height. Fixed thresholds of 2 km and 5 km were chosen as the reception height. The residence time - the time an air parcel spent over

a specific surface and below the reception height – gives indications of the aerosol characteristics of the air parcel. The method applied for Dushanbe, Tajikistan, involves seven custom defined areas as polygons, which were selected in the course of this research and are shown in Fig. 2.5. The locations are named according to their geographical context *Central Asia*, *North East Asia*, *Europe*, *Persia*, *Arabian Peninsula*, *India* and *Sahara*. The residence times at each time and height step are summed for each land cover class or polygon, where the air parcel was below the reception height. The residence times for each category and each height are visualized as profiles.

2.5 Model-reanalysis-retrieved CCN concentrations

Block et al. (2024) derived CCN number concentrations from aerosol mass mixing ratios from the Copernicus Atmosphere Monitoring Service reanalysis (CAMSRA), which were used for comparison in Sect. 3.3. The reanalysis was produced by ECMWF (European Centre for Medium-Range Weather Forecasts) within the framework of the European Copernicus program to provide information on aerosol particles, trace gases and greenhouse gases combined with operational numerical weather prediction.
The model reanalysis CCN dataset (Block, 2023) contains 3-D CCN number concentrations of global coverage for different supersaturations and aerosol species between the years 2003—2021 with daily values at a resolution of $0.75° \times 0.75°$ and 60 vertical levels.
The five aerosol species are sulfate aerosol, hydrophilic and hydrophobic black carbon, hydrophilic and hydrophobic organic matter, mineral dust and sea salt.
However, mineral dust was excluded for the CCN number concentration retrievals, because CAMS marks this aerosol type as insoluble, and no internal mixing is enabled which could enable dust to act as CCN. Another reason why dust was excluded is that Chen et al. (2020) stated that the hygroscopic properties of mineral dust remain highly uncertain due to its low hygroscopicity and non-sphericity. Additionally, it was assumed that mineral dust has small contributions to CCN due to its large size and low hygroscopicity.
After the number concentration for each aerosol type was computed, a modified kappa-Köhler theory was applied to compute the amount of aerosols that act as CCN for specific supersaturations (Block et al., 2024).

2.6 Spaceborne-lidar-retrieved CCN concentrations

Additionally, the ground-based lidar CCN retrievals are compared to spaceborne lidar CCN retrievals, which are decribed by Choudhury and Tesche (2023a,b). The polarization lidar CALIOP (Cloud-Aerosol Lidar with Orthogonal Polarization), which was onboard the sun-synchronous polar-orbiting satellite CALIPSO (Cloud-Aerosol Lidar and Infrared Pathfinder Satellite Observations), measured aerosol and cloud property profiles which range from the surface to 30 km above mean sea (m.s.l.) level (Winker et al., 2009). The lidar signals are devided into classes of aerosols, clouds, clear air, and surface. Additionally, different aerosol subtypes with their complementary modelled lidar ratios are distinguished (Omar et al., 2009). Based on the lidar ratios, the aerosol extinction and backscatter coefficients can be estimated. The horizontal resolution of the aerosol profiles is 5 km and the vertical resolution is 60 m for altitudes between 0.5 to 20 km and 180 m for altitudes higher than 20 km a.s.l.
For the retrieval of CCN products, the aerosol extinction coefficient, backscatter coefficient, and particle depolarization ratio at 532 nm wavelength and aerosol subtype classification are used. Additionally, relative humidity profiles from the Global Modelling and Assimilation Office Data Assimilation System (Molod et al., 2015) were used. The aerosol types which are part of the CALIPSO aerosol model (CAMel) consist of dust, smoke, clean continental, polluted continental, clean marine, and polluted dust. The properties of aerosol subtypes are partially based on long-term cloud-screened AERONET measurements (Omar et al., 2005), as well as other measurements (e.g., Masonis et al., 2003). In order to retrieve the corrected aerosol size distribution, the normalized size distribution from CAMel is scaled and the data is preprocessed. Afterwards, a hygroscopicity correction to account for water uptake by aerosol particles is performed and a CCN parameterization based on Mamouri and Ansmann (2016) and Tesche et al. (2009) (similar to Sect. 2.4.1) was applied. This was performed for every bin of the CALIPSO profile. In case of dust mixtures, like dusty marine and polluted dust, dust and non-dust extinction coefficients were individually passing the CCN retrieval algorithm and were then added to the total CCN concentration for each bin.

Chapter 3

Results

This chapter starts with an overview of the results of aerosol and cloud properties over the entire measurements period from 2019–2023 conducted with the PollyXT DFOV polarization lidar stationed in Dushanbe, Tajikistan. The long-term data is investigated regarding seasonality and based on these results, ACI were then assessed with consideration of the environmental situation and the temporal scale.
Then, three selected case studies are shown in detail, providing insights into single cloud microphysical properties and the complementary aerosol and atmospheric conditions.
Lastly, a comparison between CCN concentrations in Tajikistan retrieved from satellite-based lidar measurements with CALIOP on CALIPSO, model-based CAMS data, and the PollyXT ground-based lidar is presented.

3.1 Long-term statistical analysis

To study the aerosol-wind-cloud relation, different perspectives were adopted, going from a seasonal view towards the short-scale.
With regard to these results, aerosol and cloud properties were investigated and as a measure for their relationship, the ACI index was calculated.
To complement the aerosol information, a statistical analysis of the source regions for air masses that are transported to Dushanbe was conducted.

3.1.1 Seasonality of aerosol, clouds and meteorological situation

First to consider is the convective situation in Dushanbe. Profiles of pressure, temperature and humidity from GDAS were used to assess the atmospheric stability represented by the Brunt-Väisälä-Frequency N_{BVF}, in Fig. 3.1 (c). The driven parameter for N_{BVF} is the temperature gradient ∇T. Additionally, from the humidity means, a correcting factor r_{wet} was calculated based on Choudhury and Tesche (2022a), to account for hygroscopic growth due to water uptake by aerosol particles. During winter, ∇T is smallest, and

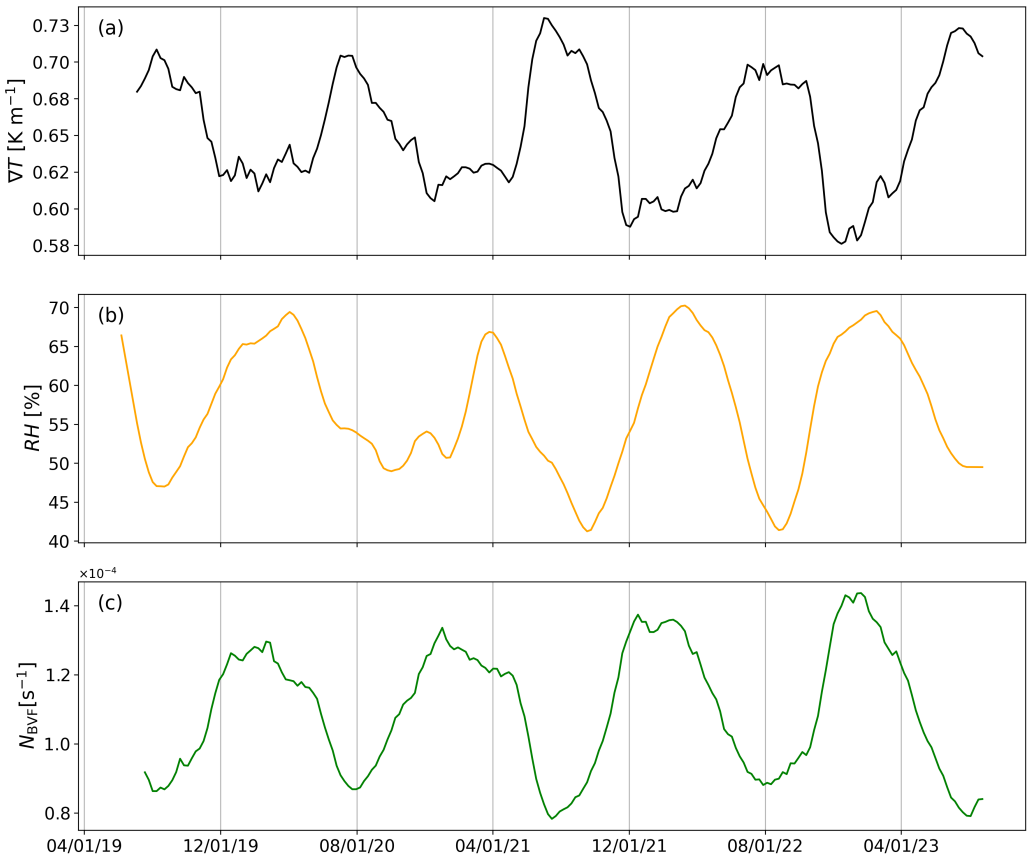

Figure 3.1: Based on GDAS profiles from 01-01-2019 to 12-31-2023 at 39° N 68° E (a) the weekly mean temperature gradient ∇T, (b) the weekly mean relative humidity, and (c) the weekly mean Brunt-Väisälä frequency N_{BVF} up to 5 km.

complementary to this, the atmospheric stability values are highest, which is unfavorable for vertical transport in the atmosphere. During summer, the

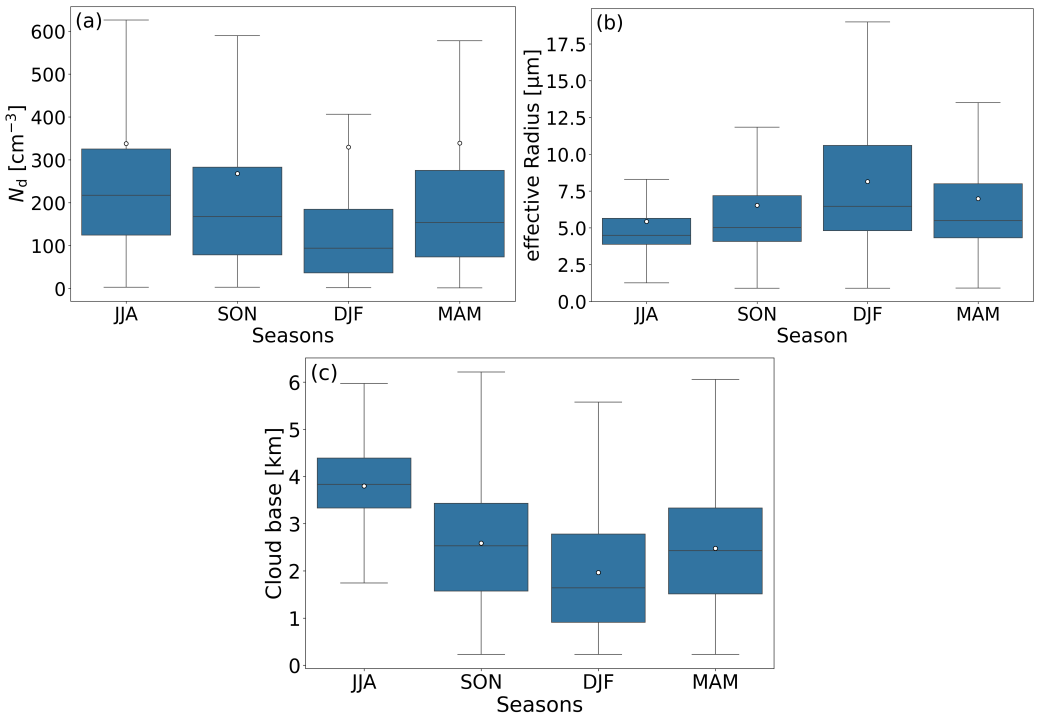

Figure 3.2: Boxplots showing the distribution of cloud properties for the four seasons (JJA = summer, SON = fall, DJF = winter, and MAM = spring) in Dushanbe measured with PollyXT during 28 months between 2019–2023. Each boxplot spans from the first quartile to the third quartile (blue box) and shown are the mean value (white circle), the median (black line), and the absolute minimum and maximum values (extended lines outside blue box) for (a) the cloud droplet number concentration (N_{d}), (b) the cloud droplet effective radius (R_{eff}), and (c) the cloud base (CB).

RH is lowest which indicates low moisture in the atmosphere. The weekly mean N_{BVF} has lowest values during summer as well, but no negative values are observed. Seasonally resolved cloud properties are shown in Fig. 3.2. During winter, the droplet number concentrations are in the lowest range of values with a median N_{d} of 94.01 cm^{-3} and the effective radius is the highest with a mean value of 8.15 µm. These observations emphasize that during winter, when it is more stable, less but larger droplets are present. In summer, the cloud droplet number concentrations are highest with a median number concentration of 217.53 cm^{-3}, and low mean effective radius of 5.42 µm, which indicates that the majority of liquid water clouds are rather unfavorable for precipitation, because the droplets are too small. Additionally, as expected, the cloud base is the lowest in winter at a mean height of 1.97 km and highest

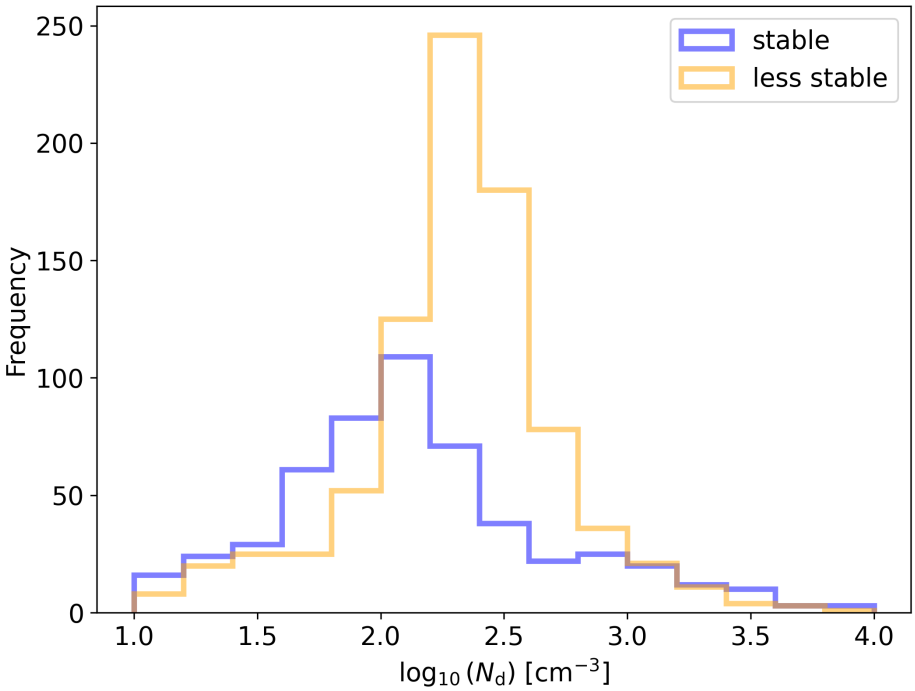

Figure 3.3: Histogram of the frequency of occurrence of cloud droplet number concentrations for stable (blue) and less stable (orange) atmospheric conditions in Dushanbe measured with PollyXT during 28 months between 2019–2023. The time periods of stable atmospheric conditions were selected to start each year on 1 December and end 1 March.

in summer at a mean height of 3.80 km.
Since less stable atmospheric conditions indicate more vertical movement in the atmosphere, which is favorable for the activation of droplets, periods of lower atmospheric stability were selected to investigate aerosol and cloud interactions. The first consideration is the effect of stability on the cloud droplet number for the whole data set. The N_d was compared for stable and less stable conditions and is shown in Fig. 3.3, which shows the logarithmic distribution of N_d. Overall, during less stable conditions, N_d is higher than during stable conditions. These differences expose a link between the stability and the cloud properties.

3.1.2 Aerosol-cloud interaction index

To search now for the aerosol effect, the aerosol-cloud interaction index, described in Sect. 2.4.4, was computed using as input the single clouds

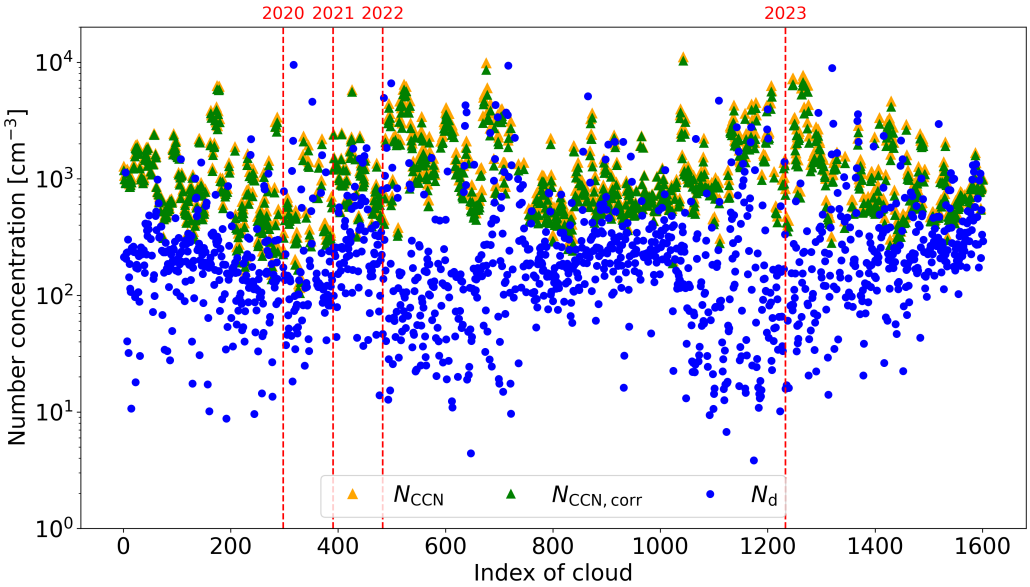

Figure 3.4: Mean number concentrations for each of the 1062 clouds that have been observed during the 28 months of measurements with PolyXT between 2019–2023 in Dushanbe. The mean cloud droplet number concentrations are depicted as blue circles, and the mean of the two-day before and after the cloud event estimated CCN number concentrations are depicted as orange triangles. The CCN number concentrations corrected for hygroscopicity growth are shown as green triangles. The red vertical lines indicate the beginning of each year.

identified in the data set. The mean N_{CCN} and N_{d} for all detected 1602 liquid water clouds is shown in Fig. 3.4, together with the corrected CCN number concentrations $N_{\mathrm{CCN,corr}}$ based on the calculated r_{wet} to account for humidity effects on the lidar-based CCN retrieval(Choudhury and Tesche, 2022a). Throughout the measurement period, the retrieved N_{d} are much lower than the N_{CCN}. Additionally, the N_{d} is spread over a broader range of number concentrations, showing more variability than the N_{CCN}. The $N_{\mathrm{CCN,corr}}$ showed a slight reduction compared to the uncorrected N_{CCN}, given the dry conditions predominant in the region studied.
The relatively large values and the differences between observed N_{d} and N_{CCN} estimates can be explained by overall restricting atmospheric conditions given by the over abundance of particles and low available moisture. This would suggest that and updraft-limited regime prevails for this region. In the time series of the cloud droplet and CCN number concentrations two features can be noted. First during winter, the increased CCN number do

not correlate with the cloud droplet numbers, which in fact, are the lowest, showing first the low effect of aerosol conditions on droplet number during the cold season and this might be partially driven by the stable conditions that prevail in winter. From this data, the stability seems also to have an effect in the maximum supersaturation resulting in less droplets during winter. In the warmer season a sort of correlation appears. However, to keep in mind that the meteorological situation not only changes in a seasonal scale, the ACI index was calculated from shorter periods considering single-cloud averages under similar meteorological situation.
Since less stable atmospheric conditions indicate more vertical movement in the atmosphere, which is favorable for the activation of CCN particles and aerosol-cloud interaction as well, periods of lower atmospheric stability were selected to derive the ACI index. Eight periods with prevailing less stable conditions were selected for this assessment. During those periods, the mean atmospheric stability was lower than a threshold of $0.00011\,\mathrm{s}^{-1}$ and N_d and N_CCN showed similar values and similar behavior over time. The mean N_d and N_CCN during those periods, which contained between 9 to 50 clouds, are shown in Fig. 3.5. The ACI index for each period, the slope of a log-log diagram, is written as well. The periods cover different time ranges, starting from three days up to ten weeks, to investigate the influence of shorter and longer time periods when investigating ACI. During all periods the slopes are showing positive correlations between the N_d and N_CCN. The lowest value of ACI index amounts to 0.197 where only nine cloud events over the course of three days were present. The highest ACI index of 1.256 was obtained during the longest time period of ten weeks. 52 cloud events had occurred during this time. This difference emphasizes the importance of different time scales when investigating aerosol and cloud interactions. Overall, this analysis shows, that during less stable atmospheric conditions, an increased correlation between aersols and clouds can be observed, which supports the explanation of an updraft-limited regime by Reutter et al. (2009) and matches investigations of Jimenez (2021). In order to investigate aerosol-cloud interactions for medium time scales, N_d and N_CCN were averaged monthly. Based on the log-log regression of the N_d and N_CCN, the ACI index was calculated and is shown in Fig. 3.6. Months, where only few liquid water clouds occurred, were excluded. Therefore, twenty-four monthly mean number concentrations of CCN and cloud droplets were used. The resulting ACI index amounts to 0.325. Comparing this to the previous short temporal scale analysis of ACI, where the maximum was 1.256 and the minimum was 0.197, the medium temporal scale analysis can be connected to a rather low but considerable positive correlation between aerosols and clouds.

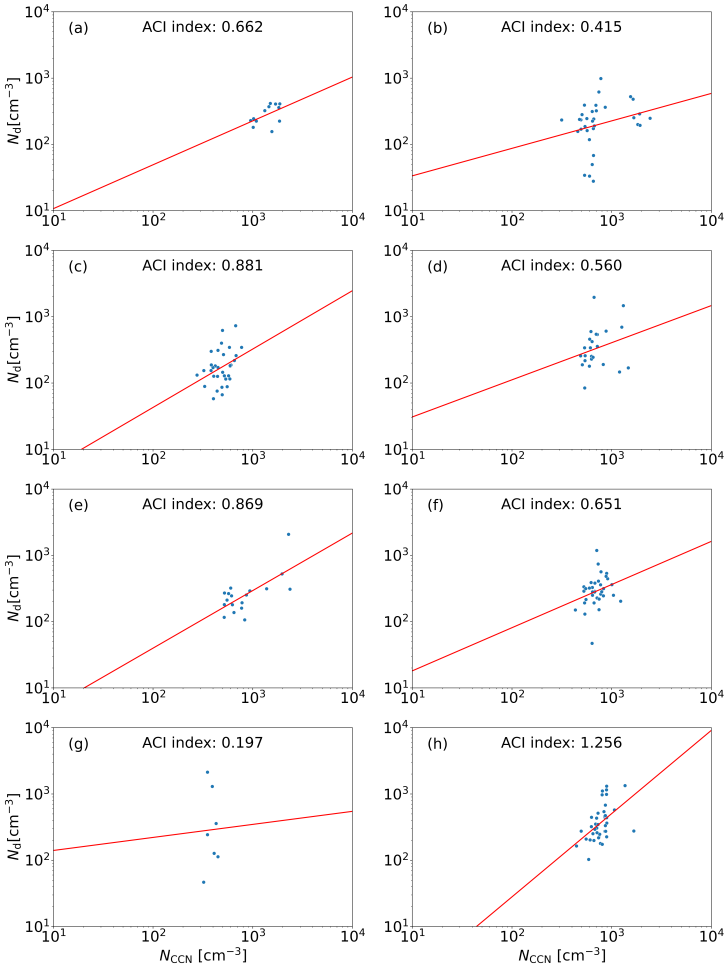

Figure 3.5: Scatter plot with mean values for each cloud of N_d and N_CCN with log-log regression (red line) to determine the ACI index. (a) 14 clouds during time period from 07-09-2019 to 08-02-2019 obtaining an ACI index $E_\mathrm{ACI}^{N_\mathrm{d}} = 0.662$. (b) 37 clouds during time period from 08-14-2019 to 09-30-2019 obtaining $E_\mathrm{ACI}^{N_\mathrm{d}} = 0.415$. (c) 37 clouds during time period from 04-21-2022 to 05-05-2022 obtaining $E_\mathrm{ACI}^{N_\mathrm{d}} = 0.881$. (d) 26 clouds during time period from 05-22-2022 to 06-03-2022 obtaining $E_\mathrm{ACI}^{N_\mathrm{d}} = 0.560$. (e) 19 clouds during time period from 06-10-2022 to 06-17-2022 obtaining $E_\mathrm{ACI}^{N_\mathrm{d}} = 0.869$. (f) 40 clouds during time period from 08-14-2022 to 10-07-2022 obtaining $E_\mathrm{ACI}^{N_\mathrm{d}} = 0.651$. (g) 11 clouds during time period from 04-02-2022 to 05-04-2023 obtaining $E_\mathrm{ACI}^{N_\mathrm{d}} = 0.197$. (h) 52 clouds during time period from 05-14-2022 to 07-30-2023 obtaining $E_\mathrm{ACI}^{N_\mathrm{d}} = 1.256$.

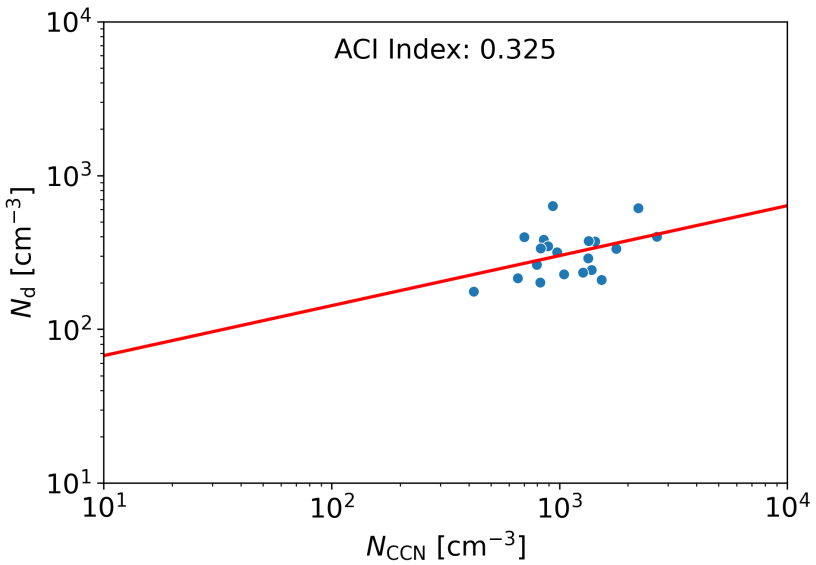

Figure 3.6: Scatter plot with monthly mean values of N_d and N_{CCN} to represent medium long periods.

To investigate larger time-periods for aerosol-cloud interactions, twelve periods were selected with each period covering multiple liquid water cloud occurrences and multiple months. The complementary mean N_d and N_{CCN} for each cloud were averaged for each period and the resulting scatter plot is shown in Fig.3.7. The ACI index for these periods is 0.549, which indicates a relatively strong influence of aerosol particles on cloud droplets. This approach emphasizes the influence of the chosen time scale when investigating ACI.

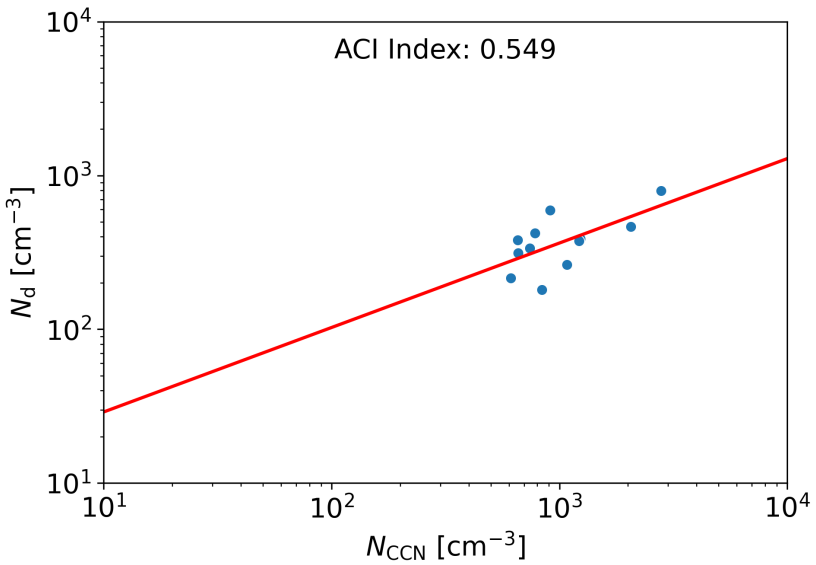

Figure 3.7: Scatter plot with mean values of N_{d} and N_{CCN} for longer periods with multiple cloud occurrences and with a log-log regression (red line) to determine the ACI index $E_{\mathrm{ACI}}^{N_{\mathrm{d}}} = 0.549$. Each point represents the averaged values of N_{d} and N_{CCN} for twelve different time periods. These periods are from 06-19-2019 to 11-03-2019 covering 154 clouds, from 12-01Figure-2019 to 01-11-2020 covering 118 clouds, from 02-06-2020 to 12-13-2021 covering 63 clouds, from 12-19-2021 to 01-03-2022 covering 28 clouds, from 03-04-2022 to 03-19-2022 covering 57 clouds, from 04-01-2022 to 05-05-2022 covering 82 clouds, from 06-18-2022 to 10-17-2022 covering 91 clouds, from 11-18-2022 to 12-09-2022 covering 73 clouds, from 12-25-2022 to 01-05-2023 covering 27 clouds, from 03-10-2023 to 04-17-2023 covering 82 clouds, from 04-26-2023 to 05-23-2023 covering 65 clouds, and from 06-01-2023 to 07-30-2023 covering 24 clouds.

3.1.3 Seasonal air mass source attribution

Previously and in the context of describing the aerosol conditions observed during the CADEX campaign (see Sect. 2.4.4), the air mass source origins in Tajikistan were investigated by individual trajectories for case studies (Hofer et al., 2017, 2020b) and seasonal cluster analysis for certain heights (Hofer et al., 2020a), only. At that time, the time-height-resolved air mass source attribution tool introduced by Radenz et al. (2021b) was not yet available. Now available and readily used (e.g.,, Radenz et al., 2021a; Floutsi et al., 2021; Hofer et al., 2024b), it was further updated with additional named geographical areas for the application to Central Asia (see Sect. 2.4.5, Lipken

et al., 2024). Motivated by the low lidar ratios at elevated depolarization ratios in background conditions (low extinction) in Dushanbe, which led to the salty dust hypothesis Hofer et al. (2020b), the new air mass source attribution tool adapted for Central Asia was already applied to investigate the layer-mean values already reported by Hofer et al. (2020b) on a case-by-case basis Hofer et al. (2024a). They found on average similar air mass origins for all cases regardless of their optical properties. However, indication of slightly more southern and south-western influenced air masses for cases with larger lidar ratios than for cases with lower lidar ratios was found (Hofer et al., 2024a).

The adapted air mass source attribution tool described in Sect. 2.4.5 and Radenz et al. (2021b) was applied for the entire measurement period and the different classifications (geographic regions: *Central Asia*, *North East Asia*, *Continental Europe*, *Persia*, *Arabian Peninsula*, *India*, and *Sahara*. Latitude bands: $> 60°$, $60° \ldots 30°$, $30° \ldots 0°$, $0° \ldots -30°$, $-30° \ldots -60°$, $< -60°$. Land surface types: *Water*, *Grass/cropland*, *Savanna/shrubland*, *Urban*, *Forest*, *Snow/ice*, and *Barren*) were investigated regarding the seasonal contribution in terms of normed residence times of air parcels for a standard reception height of 2 km arriving in Dushanbe.

Regarding the named geographical areas (Fig. 3.8a1–a4), the seasonally resolved air mass source attribution shows as expected that in all seasons, the lowest altitudes are dominated by *Central Asia* up to heights of 2 km (winter) to 6 km (summer). These are roughly the heights which Hofer et al. (2020a) reported to be the main aerosol layer heights for those seasons. *Persia* is always the second largest contribution inside this main layer, except in summer, where *Continental Europe* contribution is equal to it and also, the contribution of *Northeast Asia* is elevated (Fig. 3.8a3). Even though the air mass source attribution shows significant contributions of sources other than Central Asia in winter, upper-tropospheric aerosol layers were only detected in the non-winter seasons as reported by Hofer et al. (2020a). Such lofted layers were most distinct in spring (Hofer et al., 2020a), where above about 4 km (Fig. 3.8a2), contributions of *Persia*, *Sahara*, and *Arabian Peninsula* are found, and the latter two even dominate above about 8 km.

Regarding the latitude bands (Fig. 3.8b1–b4), again not surprisingly, contributions of *30–60* degrees are largest during all seasons, followed by *0–30* degrees. However, this is less distinct during summer, when the contribution of *0–30* degrees only becomes dominant above 8 km and even the contribution of *>60* degrees is slightly enhanced in the lowermost heights (Fig. 3.8b3).

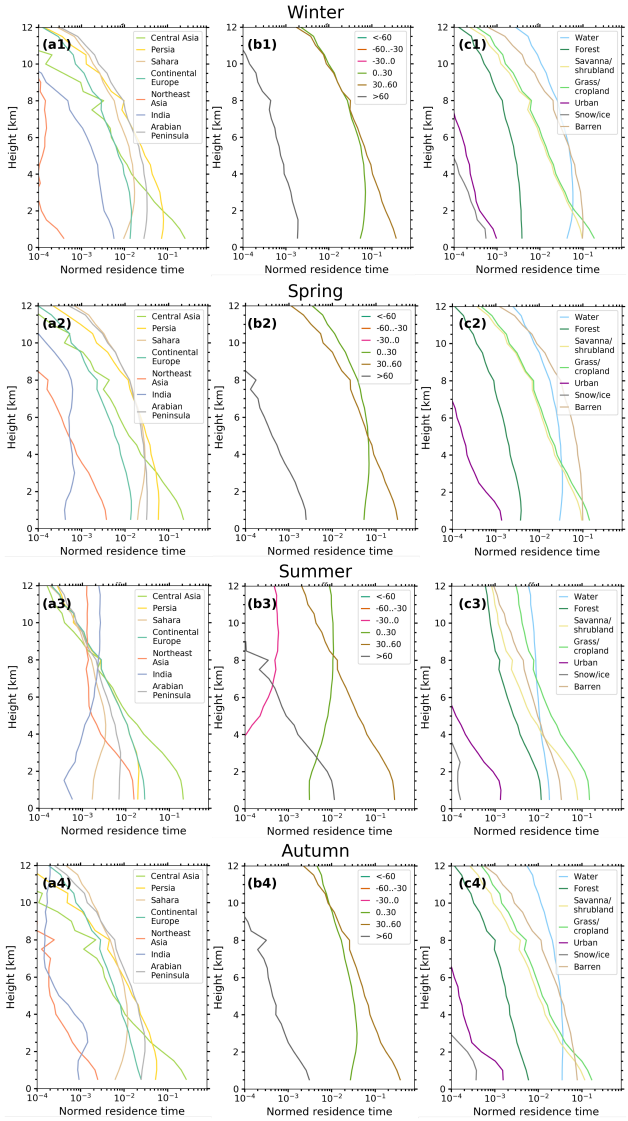

Figure 3.8: For Dushanbe from 2019–2023, seasonally resolved profiles of normed residence times of trajectories for a standard reception height of 2 km above (a) geographic regions, (b) latitude bands, and (c) land surface types for the seasons (1) winter, (2) spring, (3) summer, and (4) autumn (Radenz et al., 2021b).

Regarding the land surface types (Fig. 3.8c1–c4), *Grass/cropland* is the dominant contribution in all seasons, followed by *Barren* or *Savannah/shrubland*. In summer, inside the above mentioned main aerosol layer height up to about 4 km (Fig. 3.8c3), and to a lesser extent also in autumn (Fig. 3.8c4), *Savannah/shrubland* has a higher contribution than *Barren*. Despite occasional heavy dust outbreaks (Hofer et al., 2020a), summer and autumn are the seasons when most frequently low lidar ratios at elevated depolarization ratios during background conditions were observed (Hofer et al., 2024a).

3.2 Case Studies

Since the long-term studies showed that N_{CCN} are generally much higher than N_{d}, and dry and stable atmospheric conditions are present in Dushanbe, restricting CCN activation, three case studies have been selected to further investigate periods where a potential correlation between aerosol particles and liquid water clouds can be observed. The case studies allow the analysis of aerosol and cloud microphysical properties on a small time scale. Furthermore, the cases were selected based on different seasons, different clouds regarding height and duration, and the potential presence of ice-containing clouds was avoided.
The aerosol properties range from 500 m above the lidar, due to overlap requirements, to 300 m below the CB to exclude effects of hygroscopic growth due to humidity. The high-resolution product version after careful reprocessing, was used here. The cloud properties are representative for the cloud base region (first 75 m).

3.2.1 Case 1: 17 October 2019

As a first case the the 17 October 2019 was selected. During the measurement period from 17 October to 18 October 2019, first, a short cloud with a cloud base at roughly 3 km height was detected during late evening (Dushanbe time is coordinated universal time(UTC)+5 h), followed by a cloud that extended for roughly 9 h which had a cloud base beginning at around 2.4 km height which lofted to a height of 2.8 km at the end of the observed cloud period, which is shown in Fig. 3.9. The high resolution products show a strongly layered situation with increased particle backscatter signals. The particle depolarization ratio at 532 nm in Fig. 3.9 shows that most layers have a deplarization ratio between 0.15 and 0.20 depolarization ratio, which are typical values for polluted dust (Hofer, 2020). A remarkable feature from this case

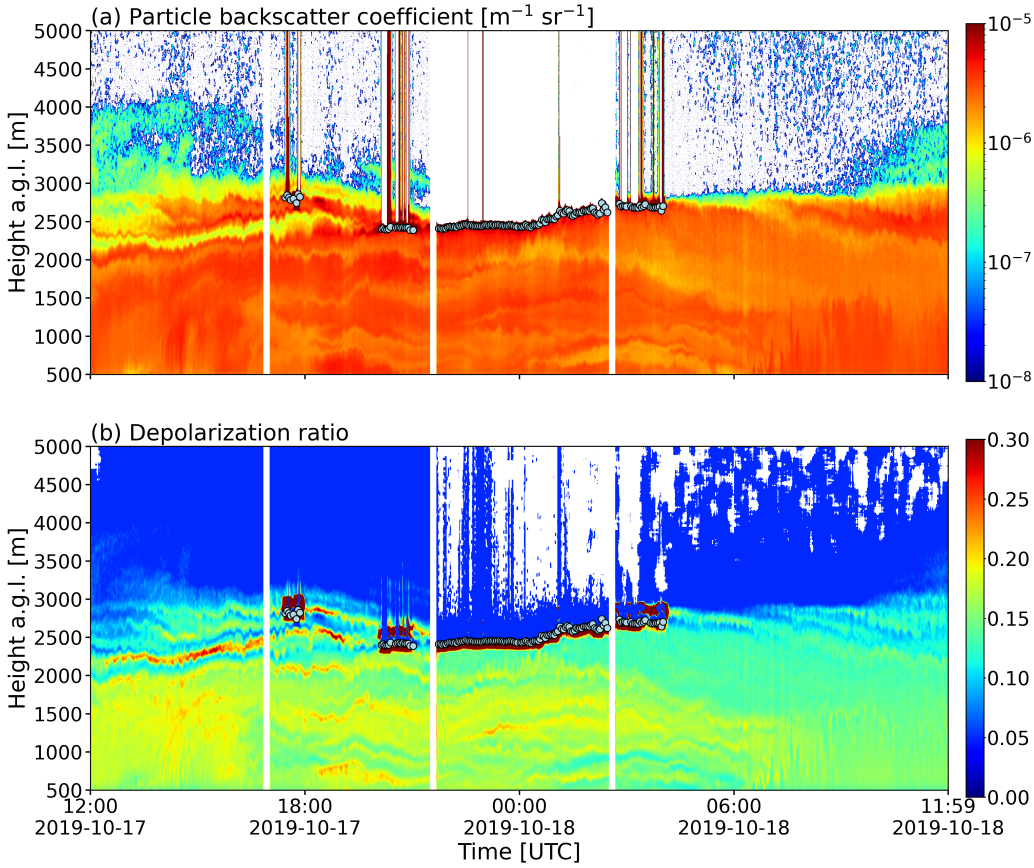

Figure 3.9: (a) High-resolution particle backscatter coefficient profile with cloud base (white circles). (b) High-resolution particle depolarization ratio with cloud base (white circles). Both profiles are for the measurement period from 12:00 UTC on 17 October to 12:00 UTC on 18 October 2019 in Dushanbe.

is the formation in the mixing of two layers during sunset, with one starting at 12 UTC at 2.2 km which is lofted towards 2.5 km before clouds occur at the same height. This aerosol layer had depolarization ratio of 0.25 – 0.30, which is typical for less polluted and rather pure dust. For a first impression about the aerosol conditions the high-quality cloud-free profiles from two days before the cloud event and up to two days after (15–17 October 2019) were averaged and are depicted in Fig. 3.10. These profiles were actually considered for the ACI analysis at larger temporal scales, see Sect. 3.1.2. They show that for the lowest 2 km, the dust backscatter coefficients was higher than the non-dust one, and at 2.5 km, the dust and non-dust backscatter

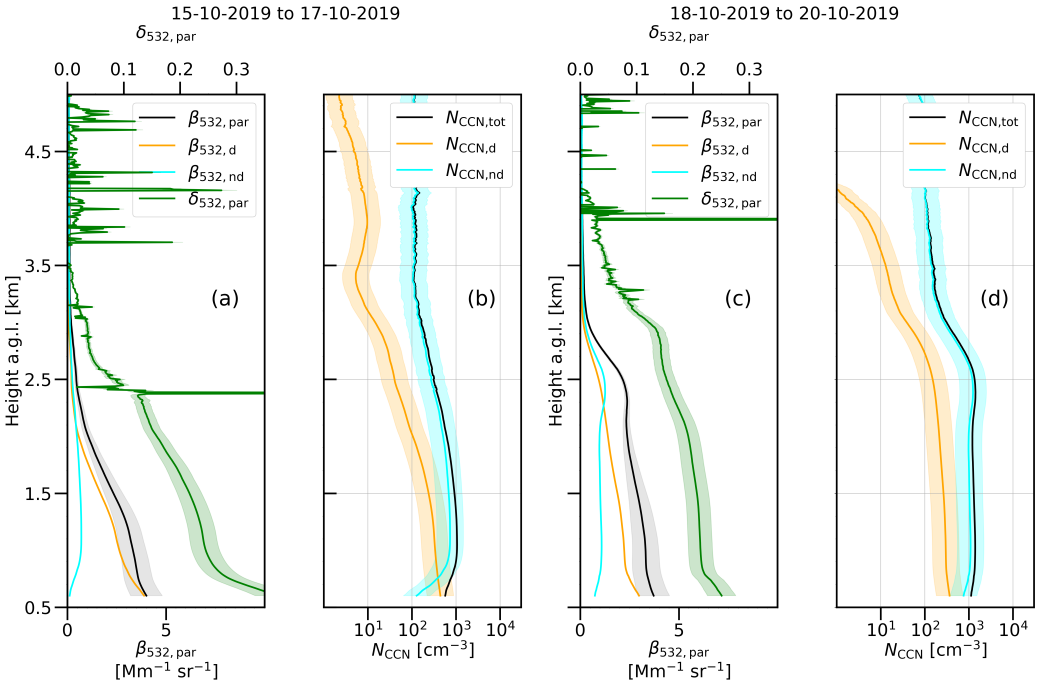

Figure 3.10: 2-day mean profiles before and after the cloud occurrence on 17 October 2019 in Dushanbe. Panels (a) and (b) show profiles before the event (15-10-2019 to 17-10-2019), while panels (c) and (d) show profiles after the event (18-10-2019 to 20-10-2019). (a) and (c) display profiles of particle backscatter coefficient (black) with the shaded region indicating the uncertainty of 20 %, dust backscatter coefficient (orange), non-dust backscatter coefficient (blue), and particle depolarization ratio (dark green) with the shaded region indicating the uncertainty of 10 %. (b) and (d) display profiles of total CCN number concentration $N_{\mathrm{CCN,tot}}$ (black), dust CCN number concentration $N_{\mathrm{CCN,d}}$ (orange), and non-dust CCN number concentration $N_{\mathrm{CCN,nd}}$ (blue) with the shaded regions indicating an uncertainty of a factor of 2.

coefficients have similar values. For the CCN concentration estimates, the non-dust contribution is assumed to be composed by continental pollution, a much better CCN than dust. The CCN number concentration estimates for a supersaturation of 0.2 % show that before the cloud, higher values of non-dust than dust CCN number concentrations were present for all altitudes, even those which had a stronger dust backscatter coefficients. The total CCN number concentration where the clouds formed at about 2.5 km were about 400 cm^{-3} the days before the cloud event and roughly over 1000 cm^{-3} the days after. These values are representative for the CCN situation at the

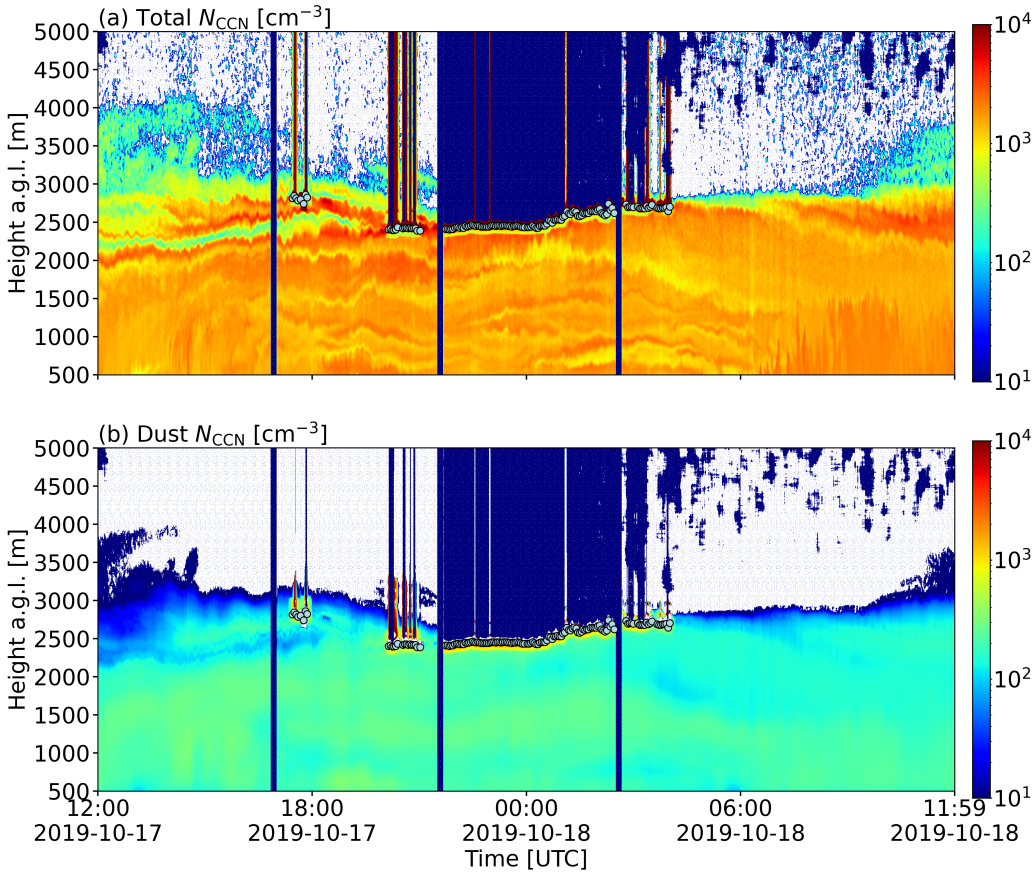

Figure 3.11: (a) Logarithmic high-resolution total CCN number concentration $N_{\mathrm{CCN,tot}}$ profile with cloud base (white circles). (b) Logarithmic high-resolution dust CCN number concentration $N_{\mathrm{CCN,d}}$ profile with cloud base (white circles). Both profiles are estimations based on the method described in Sect. 2.4.1 for the measurement period from 12:00 UTC on 17 October to 12:00 UTC on 18 October 2019 in Dushanbe.

cloud level, but help us only to see the cloud as a whole. To deepen into the evolution of the cloud situation, the high-resolution products were considered to assess the CCN in the whole boundary layer beneath the cloud. The total CCN and those originated by dust, are shown in Fig. 3.11.

To look at the aerosol-cloud covariability with numbers, an average value of the CCN concentration was designated to each cloud data bin. The dust, non-dust and total CCN number concentrations compared to N_{d} are shown in Fig. 3.12. The CCN concentrations were vertically averaged from 500 m above the ground to 300 m below the CB, and temporally over the three minutes of each cloud assessment. As it was shown in the previous section, cloud

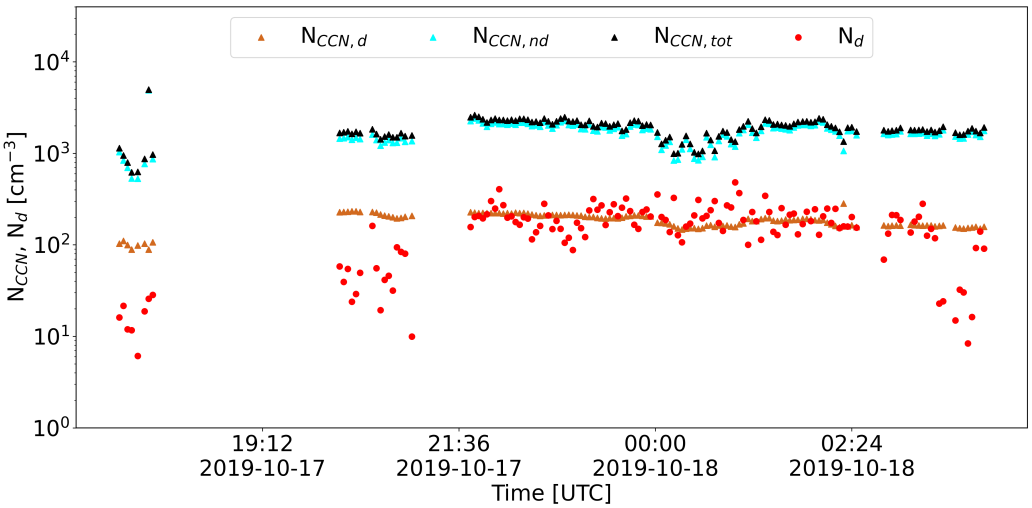

Figure 3.12: Time series during cloud occurrence from 17:00 UTC on 17 October to 05:00 UTC on 18 October 2019 in Dushanbe. The plot shows the logarithmic CCN number concentration averaged for the height between 500 m above the lidar and 300 m below the cloud base, based on the profile that was temporally closest to the cloud data point. The total CCN number concentration ($N_{\mathrm{CCN,tot}}$) (black triangles), dust CCN number concentration ($N_{\mathrm{CCN,d}}$) (orange triangles), non-dust CCN number concentration ($N_{\mathrm{CCN,nd}}$) (blue triangles), and cloud droplet number concentration (N_{d}) (red circles) for the height from the cloud base to 75 m into the cloud are shown.

properties respond to the variability of aerosol but also to the atmospheric stability. By looking at case studies in detail, i.e., to the high-resolution 3-minute information, eventually, the effect of aerosol in cloud properties within the lifetime of a single cloud, can be observed. For this case N_{d} concentrations were much lower than the CCN concentrations, but both follow a similar development of number concentration over time. Only at the beginning and the end of the cloud, N_{d} show different behavior than N_{CCN}. At the beginning and end of the cloud occurrence, also higher effective radii were measured shown in Fig 3.13, which indicates that at the beginning and end of the cloud less droplets with larger sizes were present, while during the cloud occurrence, more but smaller droplets were present. During the first short cloud, which started at 17:30 UTC, the N_{d} seems to follow the variability of the CCN, however the range of values are about one order different. This contrast is seen for the whole period. Aerosol temporal variability still seems to shape the cloud response in such short times. The CCN ranged from about 500 to 3000 cm^{-3}, while N_{d} varied between 10 and 400 cm^{-3}. As not

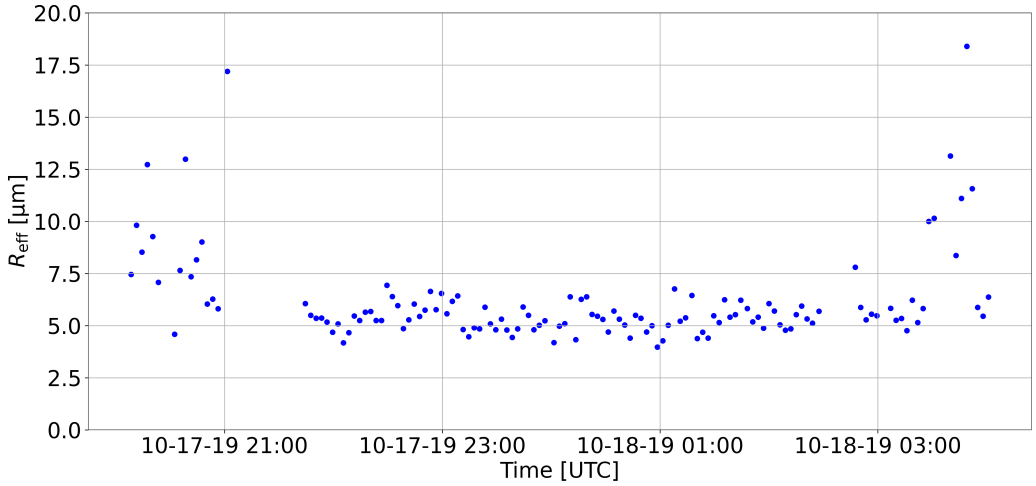

Figure 3.13: Time series of cloud droplet effective radius R_{eff} 75 m above cloud base during cloud occurrence from 17:00 UTC on 17 October to 05:00 UTC on 18 October 2019 in Dushanbe.

only aerosol conditions shape cloud microphysics, the atmospheric stability by means of N_{BVF} was considered. Between the 16 and 18 October 2019, N_{BVF} varied between the range 1 – $1.4 \times 10^{-4}\,\mathrm{s}^{-1}$. The median N_{BVF} for Dushanbe between 2019 – 2023 is about $1 \times 10^{-4}\,\mathrm{s}^{-1}$, making of this case a rather stable atmospheric situation. A potential explanation is that 0.2 % supersaturation was not reached during the winter. Additionally, during winter, the atmospheric stability is stronger, suppressing vertical motion and limiting the CCN activation (Reutter et al., 2009). In Fig. 3.14, the 3-hourly air mass source attribution profiles for different geographic regions for 17 October 2019, 11 UTC to 18 October 2019, 11 UTC is presented. Most air masses from the 10-day backward trajectories arrived at altitudes below 2 km. Most air masses at lower heights had residence times over *Central Asia*, and a smaller fraction of air masses had residence time over *Continental Europe*. Therefore, both source regions had potential to influence the aerosol situation for heights up to 2 km. Since the cloud developed from aerosol layers that reached altitudes of about 2 km, the source region attribution for heights up to 2 km gives valuable information in this case.

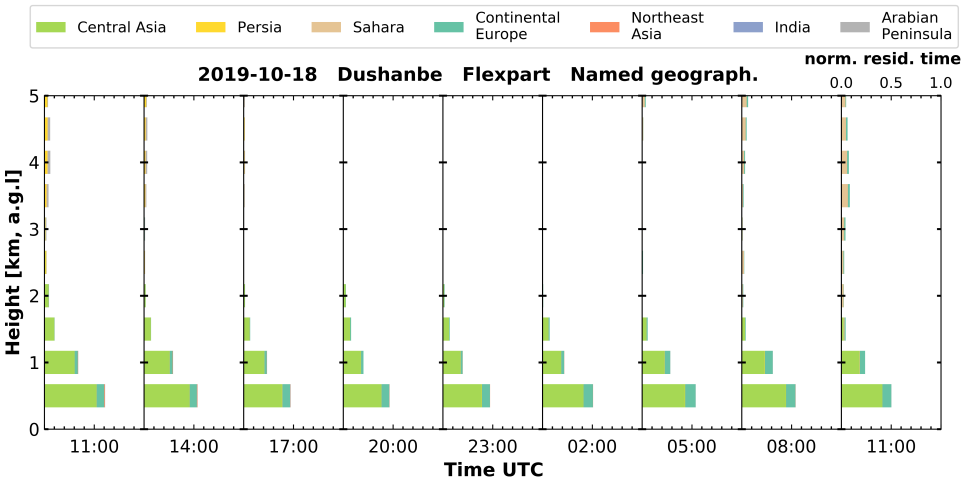

Figure 3.14: 3-hourly profiles of normed residence times of trajectories above the geographical regions *Central Asia* (light green), *North East Asia* (orange), *Continental Europe* (dark green), *Persia* (yellow), *Arabian Peninsula* (grey), *India* (blue), and *Sahara* (beige) from the temporally and vertically resolved air mass source attribution tool for 17 October 2019, 11 UTC to 18 October 2019, 11 UTC in Dushanbe.

3.2.2 Case 2: 8–10 October 2019

To investigate aerosol and cloud properties during a longer time frame, covering multiple cloud events, the period from the 8 to 10 October 2019 was selected. In Fig. 3.15, vertically high extended layers throughout the period with a first long lasting cloud from the 8 October 16 UTC to 9 October 3 UTC can be observed. Then, a short single clouds in between and lastly,

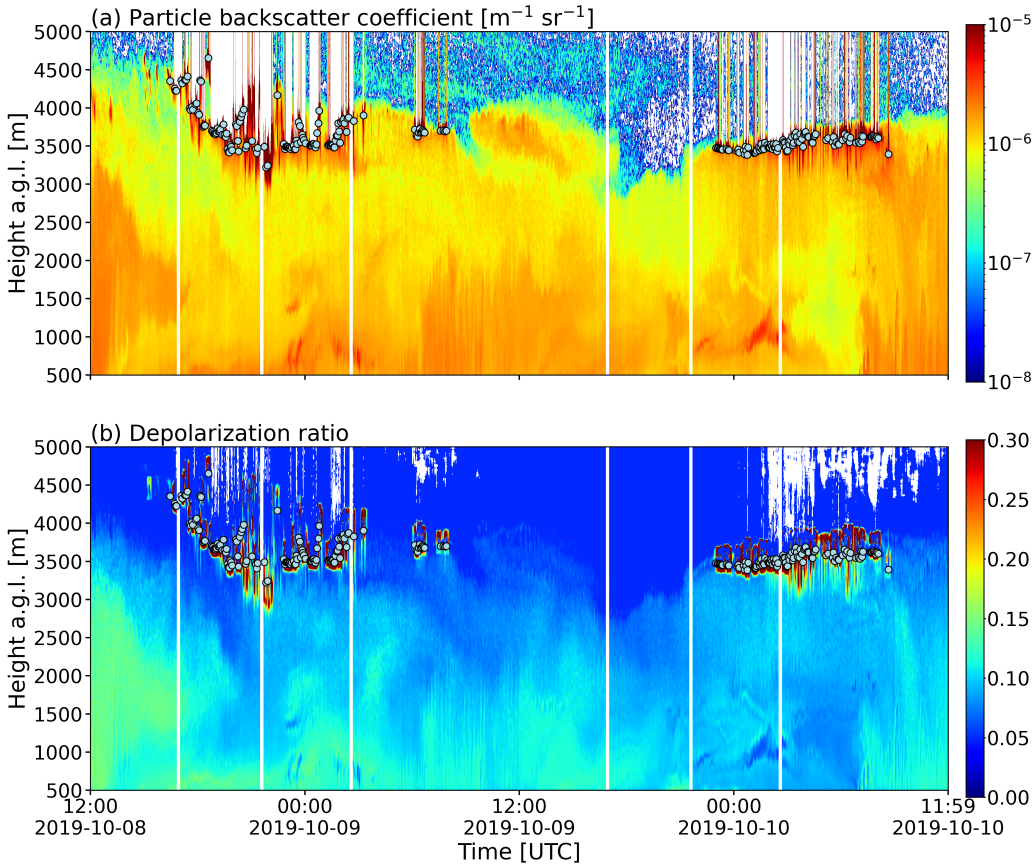

Figure 3.15: Same as Fig. 3.9, but for 12:00 UTC on 8 October to 12:00 UTC on 10 October 2019.

a longer lasting cloud from 9 October 23 UTC til 10 October 10 UTC was measured. The first detected cloud base descended starting from 4.5 km and ranges mostly from 3 to 4 km height. The second cloud during the night of the 10 October had a more stable and less vertically spreading cloud base at around 3.5 km and upwards. The particle depolarization ratio was overall low and ranges from layers with increased signals of 0.15 to periods with depolarization ratios lower than 0.10. In Fig. 3.16, the aerosol conditions of

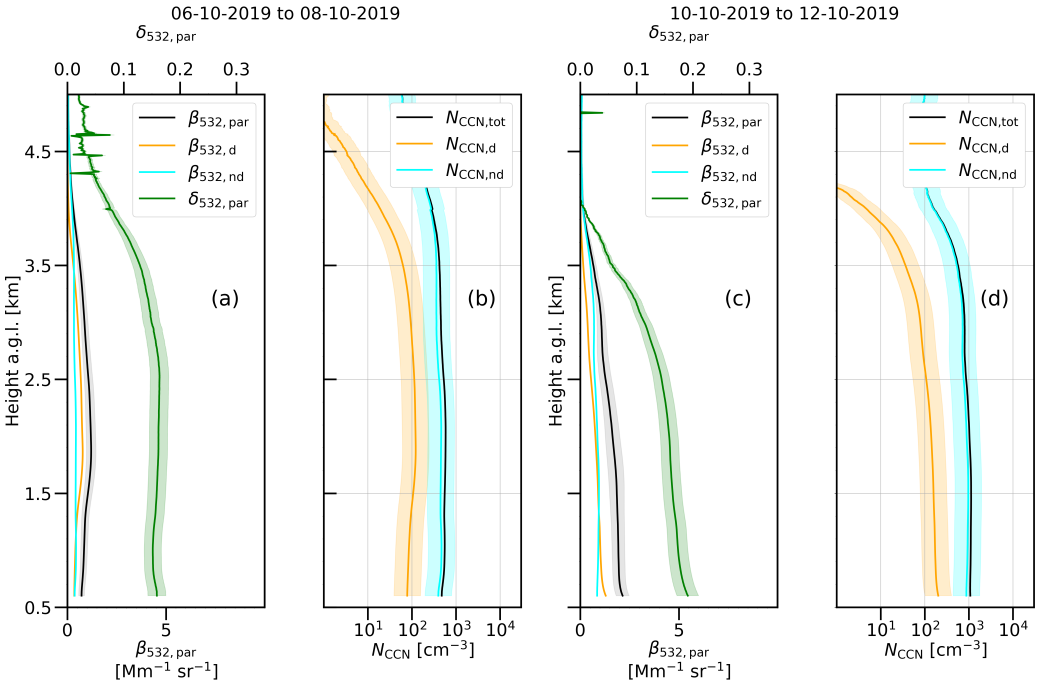

Figure 3.16: Same as Fig. 3.10, but with (a) and (b) averaged for time period 6 to 8 October 2019, and (c) and (d) for 10 to 12 October 2019.

the 2-day mean before the cloud event are shown. It shows stronger dust backscatter coefficients at lower altitudes and reversed for altitudes higher than 3 km. The CCN number concentrations were in a similar range as for the 17 – 18 October 2019 and again strong contribution from non-dust and rather low from dust.As shown in Fig. 3.17, the droplet number concentrations varied more during the first cloud event, with complementary varying CCN conditions during that first time period. Here, the dust CCN number concentrations showed the strongest increase and rather small changes in N_{d}. The second cloud had more constant number concentrations. During periods where the CCN number concentrations had small variability, the cloud droplet number concentrations did not show the same behavior. Although the 3-minute pieces showed strong variability but no strong correlation, between the first two cloud periods a slight decrease in the N_{CCN} and N_{d} can be noted, then increase again in the third period during the night. N_{BVF} for this case varied between 0.7 to $1.0 \times 10^{-4}\,\mathrm{s}^{-1}$, indicating lesser stability than the first case 10 days later. In fact, the CCN concentrations were on a similar range, compared to the first stable case, of 600 – 2000 cm^{-3}. For these less stable days, N_{d} mostly varied between 300 – 800 cm^{-3}, indicating a higher activation rate, likely due to stronger updrafts. The ACI index was

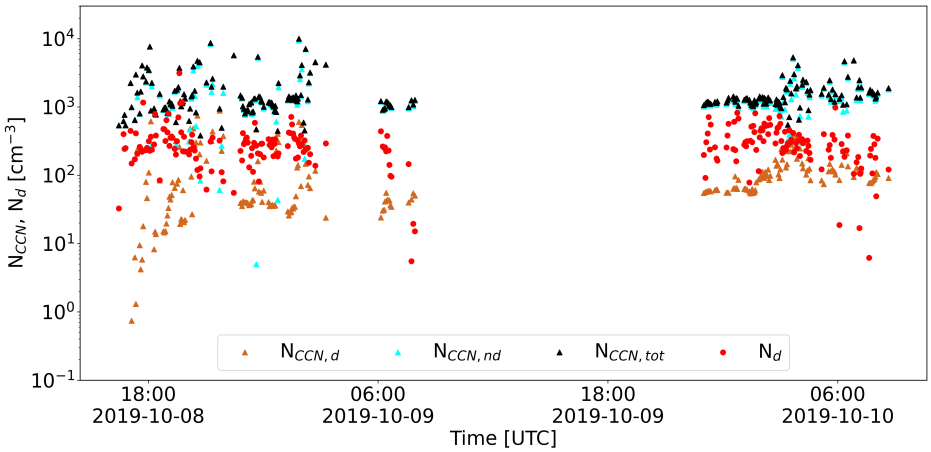

Figure 3.17: Same as Fig 3.12, but for 18 UTC on 8 October to 10 UTC on 10 October 2019.

calculated for this case and amounts to 0.358.
In Fig. 3.18, the 3-hourly air mass source attribution profiles for different geographic regions for 9 October 2019, 11 UTC to 10 October 2019, 11 UTC is presented. It shows that for the lowest 2 km, most air masses had residence times over *Central Asia*. Contributions from *Persia* were also present throughout the whole time period and dominating for altitudes above 2 km.

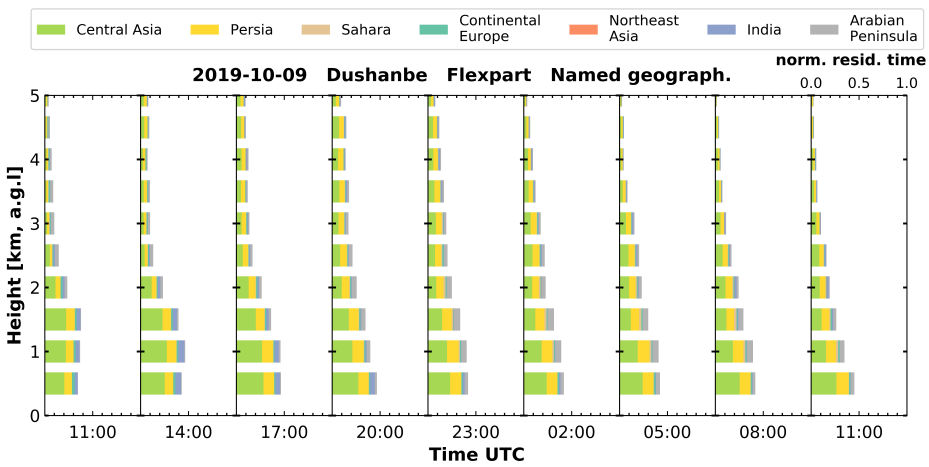

Figure 3.18: Same as Fig. 3.14, but for 9 October 2019, 11 UTC to 10 October 2019, 11 UTC.

3.2.3 Case 3: 1 June 2023

The third cloud event that was selected for this study was detected during summer on 1 June 2023. During summer, the atmospheric conditions are least stable compared to the rest of the year based on the long-term analysis (see Fig. 3.1). The particle backscatter coefficient profile and particle depolarization ratio are shown in Fig. 3.19. The cloud base is between 4 to 4.5 km. During the night, multiple cloud sections over the course of 6 h with a cloud base at an altitude first at 4.5 km and then at roughly 4 km were detected. The particle backscatter coefficient at 532 nm shows an aerosol layer at 4 km and a layer that was lifted towards 4 km where the last cloud snippet started to form.

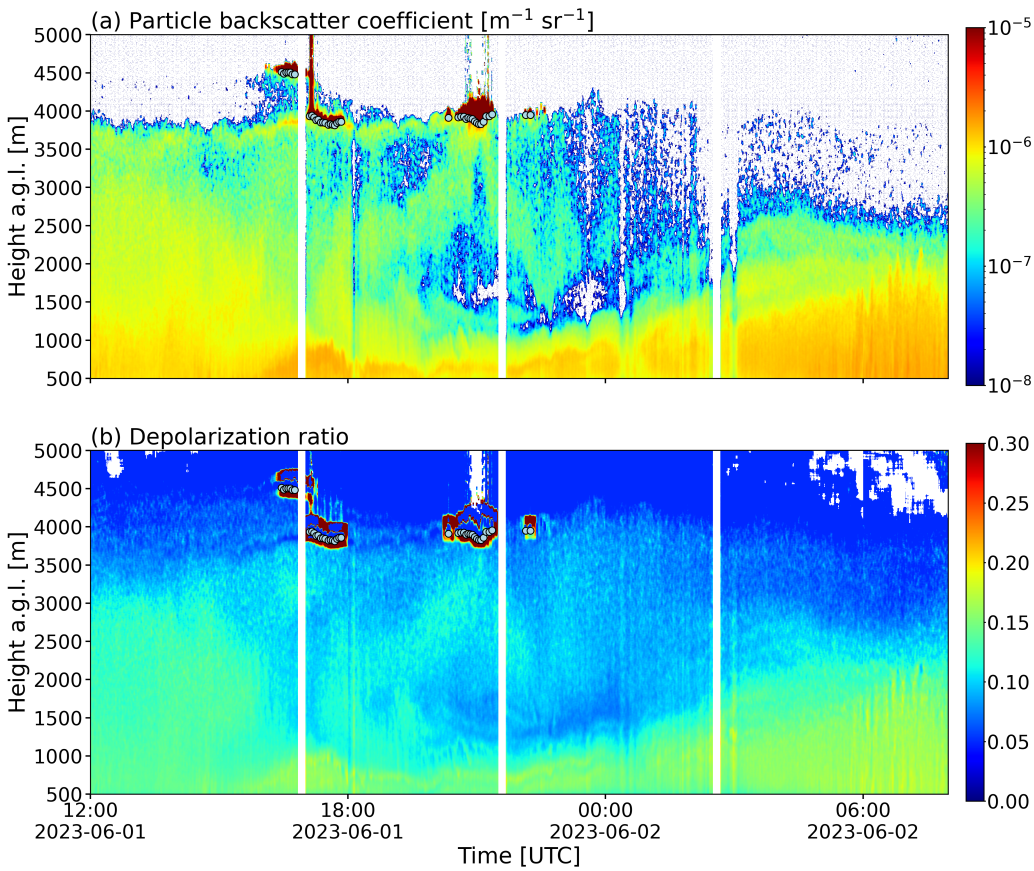

Figure 3.19: Same as Fig. 3.9, but for 12:00 UTC on 1 June to 8:00 UTC on 2 June 2023.

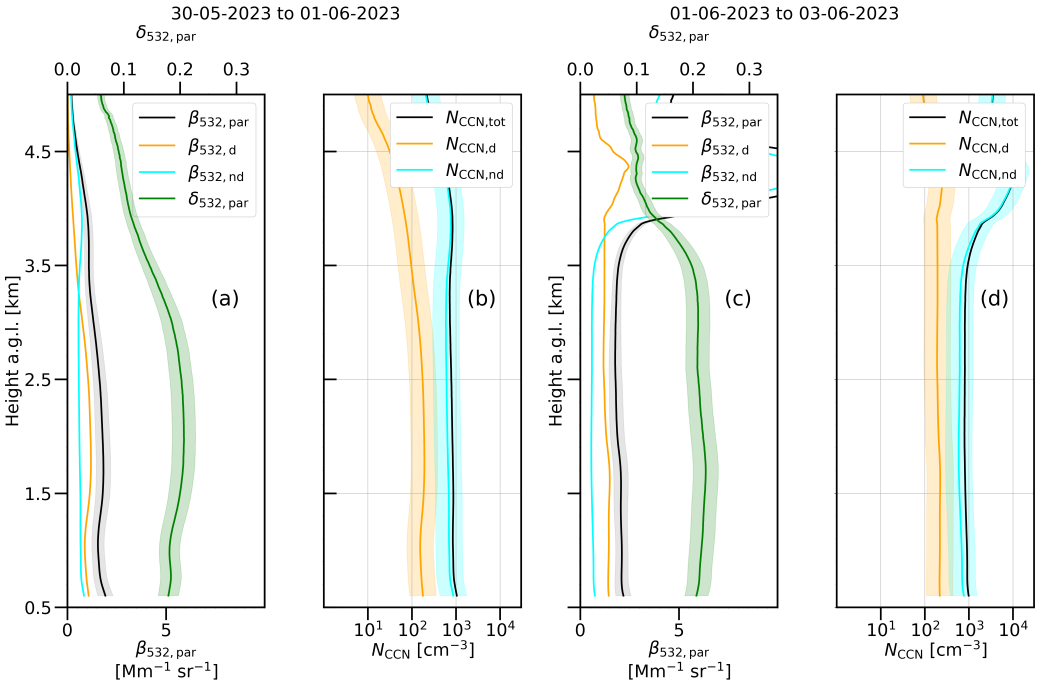

Figure 3.20: Same as Fig. 3.10, but with (a) and (b) averaged for time period 30 May to 1 June 2023, and (c) and (d) for 1 to 3 June 2023.

The averaged profiles from two days before and after the cloud occurrence, shown in Fig. 3.20 contain the backscatter coefficient for dust and non-dust. For dust, the value is higher up to 3.5 km height, but at higher altitudes the non-dust backscatter coefficient is higher. Depolarization ratios are enhanced to about 0.2 up to 3 km height, only, with lower depolarization ratios higher up. This indicates the presence of polluted or salty dust mixtures. The CCN number concentration of non-dust is overall higher at all altitudes than the dust CCN number concentration which is shown in Fig. 3.21. In Fig. 3.22, the time series of the beneath-cloud CCN and cloud droplet number concentrations is shown. For this summer case, the N_{CCN} and N_{d} were found in a similar range of 200 – 400 cm^{-3}. Even higher values of N_{d} were found at the beginning of the event, reaching the N_{d} maximum values over 1000 cm^{-3}. This situation comes along with a less stable situation, with N_{BVF} of about 0.6 – 1.0 $\times 10^{-4}$ s^{-1} during the 1 June 2023. After the detection of the first high cloud at 4.5 km, the droplet number concentration decreased and became similar to the total CCN concentration. Overall, the droplet number concentration varies more strongly over time than the CCN number concentrations. The air mass source attribution regarding geographical areas (see Sect. 2.4.5) for the 1 June 2023 is shown in Fig. 3.23. For the lowest 2.5 km,

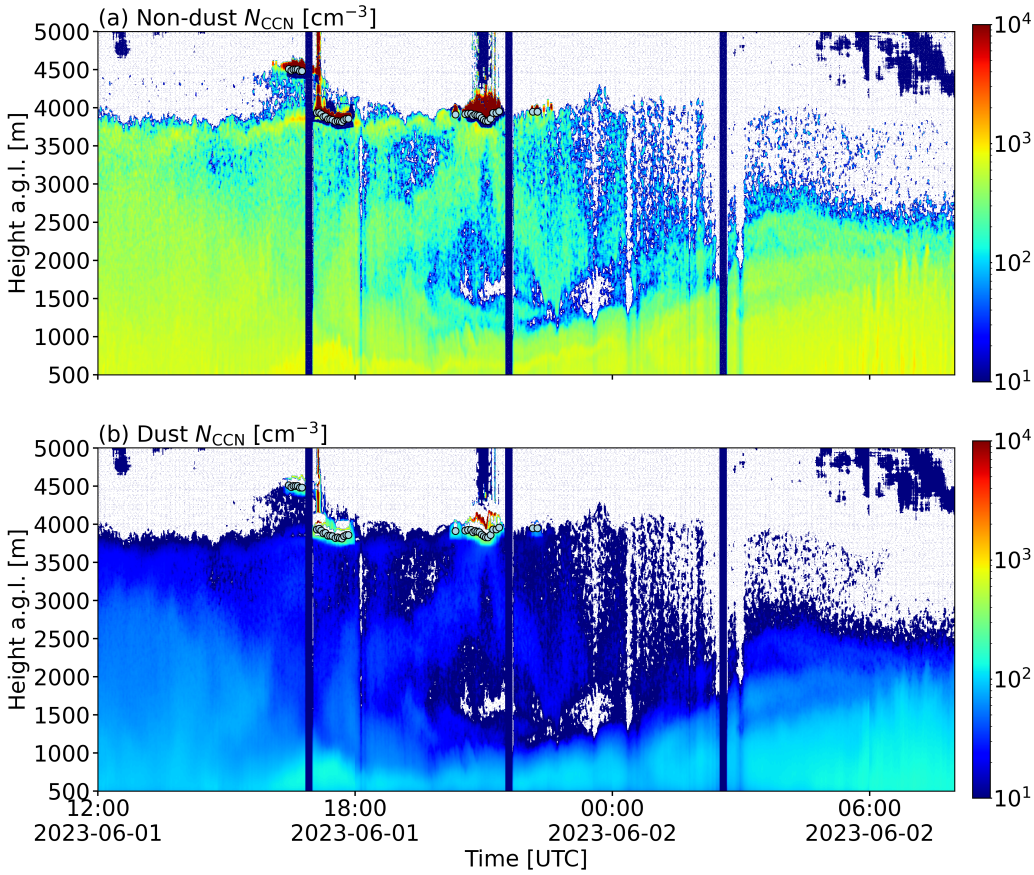

Figure 3.21: (a) Logarithmic high-resolution non-dust CCN number concentration $N_{\mathrm{CCN,nd}}$ profile with cloud base (white circles). (b) Logarithmic high-resolution dust CCN number concentration $N_{\mathrm{CCN,d}}$ profile with cloud base (white circles). Both profiles are estimations based on the method described in Sect. 2.4.1 for the measurement period from 12:00 UTC on 1 June to 8:00 UTC on 2 June 2023.

the source region Central Asia was the most dominant throughout the whole day. At altitudes above 3 km, the source regions are *Sahara* and *Arabian Peninsula* which potentially caused an increased number of dust particles at ranges up to 4.5 km.

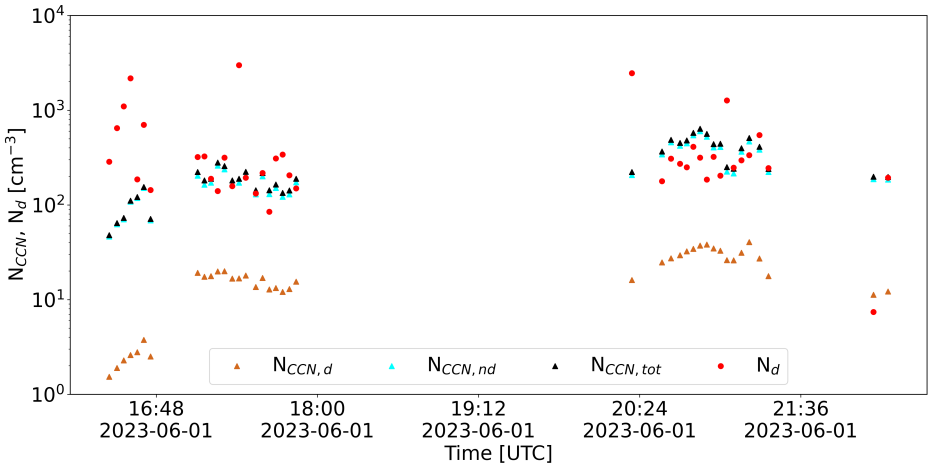

Figure 3.22: Same as Fig 3.12, but for 1 June 2023.

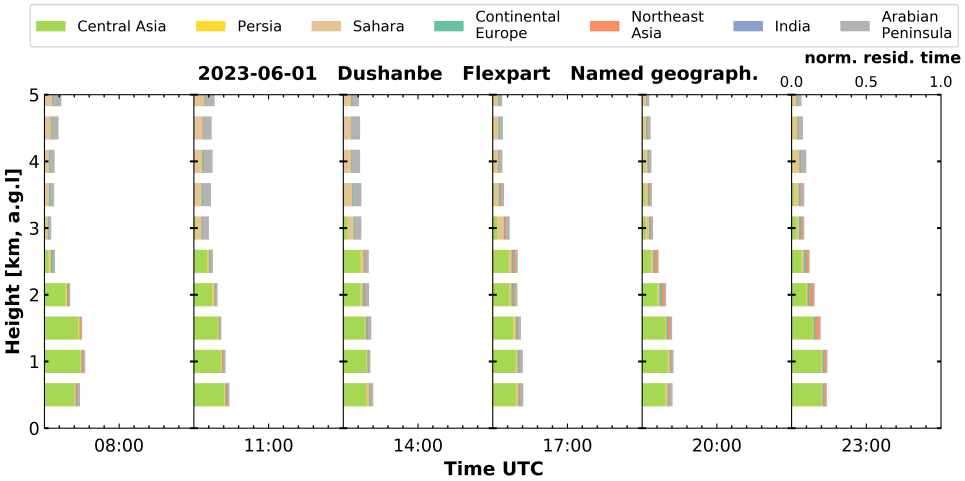

Figure 3.23: Same as Fig. 3.14, but for 1 June 2023.

With the characterization of the aerosol and cloud situation, along with atmospheric stability, the relationship of aerosol and cloud properties was studied in detail. The ACI index was evaluated for different temporal scales, going from studying cloud changes over different days, months, and seasons. The high-resolution information was also used to investigate cloud evolution within single cloud periods corroborating the general link between stability, CCN concentration (at a given supersaturation) and cloud droplet concentration, which could potentially help us to further investigate cloud processes involved with the adjustments associated to the instantaneous aerosol-cloud effect.

3.3 Comparison with CALIPSO- and CAMS-retrieved CCN number concentrations

Lastly, a comparison with the CCN concentrations from CALIPSO and CAMS reanalysis, reported by Choudhury and Tesche (2023a) and Block et al. (2024) is presented in this section.

Many studies in this region rely on CALIPSO measurements (e.g., Li and Sokolik, 2018; Liu et al., 2019; Wu et al., 2022; Han et al., 2022; Gan et al., 2024), which emphasizes the need for quality checks of this satellite-based data. While the ground-based lidar can conduct continuous measurements at a fixed location, the satellite orbits the globe, which enables fewer measurements at the same location. Additionally, one goal of experimental studies is to utilize them as input data for models. Comparing the measured CCN to a model where dust was neglected as CCN can give important knowledge about the situation in Central Asia.

For CALIPSO, the data from the coordinates 38 N, 67.5 E was used. For CAMS, data from 38.23 N, 69 E at the model levels 42 to 60 was selected. Both, the data from CALIOP and CAMS CCN concentrations are covering the time period from 2019–2021. The ground-based PollyXT lidar measurements were conducted between 2019–2023, but from February 2020 to October 2021 the lidar was unable to measure, which needs to be considered when comparing these observations to the two datasets from 2019 to 2021.

Block et al. (2024) validated their CAMS-retrieved near-ground CCN concentrations against rather short-term ground-based in situ observations of multiple ARM sites (Atmospheric Radiation Measurement, U.S. Departement of Energy, e.g.,, Stokes and Schwartz, 1994; Uin et al., 2019). They found good agreement between CAMS and in situ CCN values, however, with largest overestimation by CAMS for highly polluted areas (Block et al., 2024). They state that larger organic matter AOT in the Northern Hemisphere in the new CAMS model (Inness et al., 2019) might be a reason for this bias and further validations are needed. Furthermore, as only validation with near-ground values was performed, efforts on a more detailed validation, than the bulk one presented here, in the vertical dimension should be spent. The same should be done for the CALIOP-retrieved CCN profiles as well. The Dushanbe dataset is suitable for these tasks, but they are beyond the scope of this thesis.

A first comparison of the CCN number concentration estimations of the ground-based PollyXT lidar, the satellite-based CALIOP lidar, and model-based CAMS reanalysis CCN is shown in Fig. 3.24. The comparison shows a good agreement between all CCN number concentration estimates for

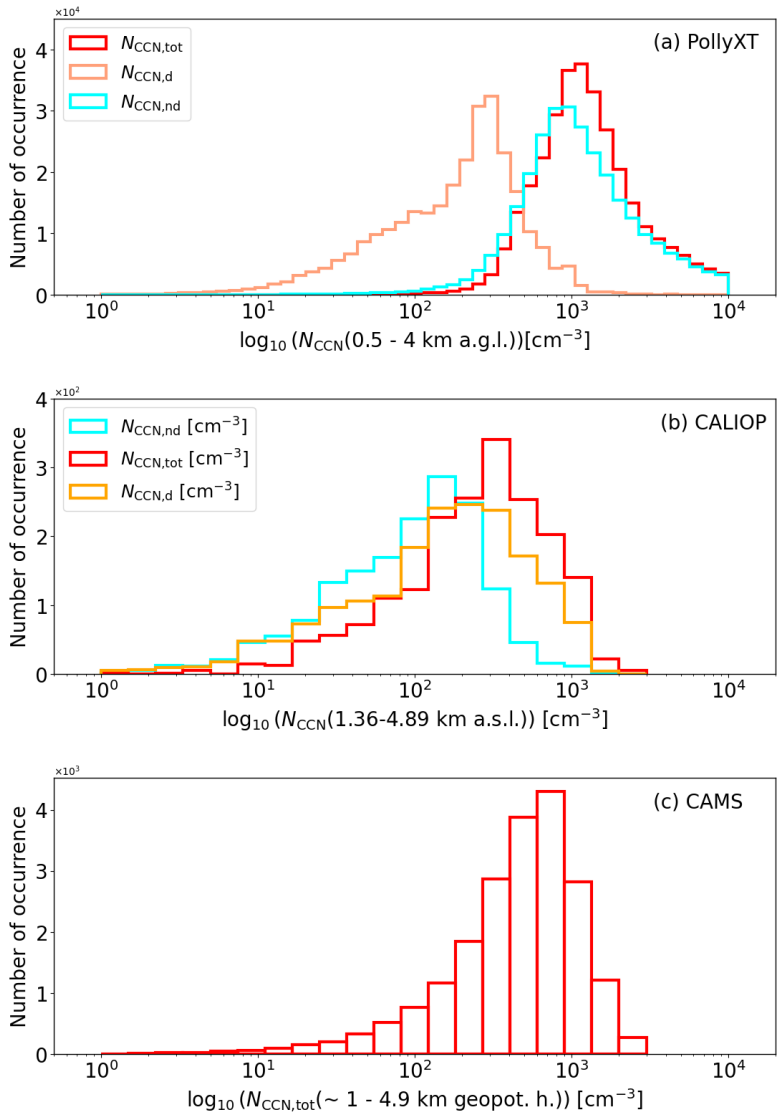

Figure 3.24: Histograms of logarithmic CCN number concentrations N_{CCN} of all observed points based on (a) the ground-based PollyXT lidar, (b) spaceborne lidar CALIOP, and (c) model-based CAMS reanalysis. (a) At 38° 33′ 34″ N, 68° 51′ 22″ E, based on all available measurements during 2019–2023, with a number of occurrences in the range of 10^4, vertically averaged from 0.5 km to 4 km a.g.l., separated into total (red), dust (orange), and non-dust (blue) N_{CCN}. (b) During 2019–2021 for the location 38 N/67.5 E, with a number of occurrences in the range of 10^2, vertically averaged from 1.36 km to 4.89 km a.g.l., separated into total (red), dust (orange), and non-dust (blue) N_{CCN}. (c) Total N_{CCN} for 38.23 N/69 E during 2019–2021, with a number of occurrences in the range of 10^3, vertically averaged from 1 km to 4.9 km (levels 42–60) geopotential height.

Dushanbe.
The satellite-based CCN concentrations in Fig. 3.24(b) are shifted to overall lower values, and the contribution of dust CCN is higher than the non-dust contribution. Based on the ground-based CCN analysis, the opposite is observed, retrieving higher non-dust CCN than dust CCN number concentrations.
The difference between the satellite-based and ground-based lidar retrieved CCN concentrations might be caused due to clouds covering atmospheric layers below, where pollution and other non-dust aerosols are emitted, and due to the view point of the satellite from above, more of the non-dust aerosols are not measured. Since many studies have shown that dust can reach high altitudes, which allows the dust to be transported further distances, sourcing from Sahara and Arabian Peninsula, such dust concentrations might layer on top of clouds, which would increase the dust CCN concentrations retrieved with a satellite-based lidar (e.g., Shukurov et al., 2023). Previous comparison studies showed that POLIPHON-retrieved CCN values are generally higher than CALIOP-retrieved ones and the latter are higher than ground-based in situ measured ones (Choudhury and Tesche, 2022b). Choudhury and Tesche (2022b) found worst agreement of CALIOP-retrieved, and as well of POLIPHON-retrieved, with in situ retrieved CCN values for a dust-influenced Mediterranean station. They state changes in the microphysical properties of the aerosol types caused by chemical or cloud processing, and the assumption of dust being hydrophobic as possible reasons for this disagreement. However, other than in Tajikistan, dust and marine aerosol mixtures were likely the main CALIOP-detected aerosol type for this station. For such mixtures, Choudhury et al. (2022) reported as well disagreements between airborne in situ and CALIOP-retrieved CCN concentrations, while generally finding moderate agreement for dust-dominated retrievals. Both studies (Choudhury et al., 2022; Choudhury and Tesche, 2022b) also mention large variability might be caused due to differences between nighttime and daytime satellite tracks and sensibility. Overall, the differences between satellite-based and ground-based lidar retrieved CCN concentrations need to be further investigated.

Chapter 4

Summary and Outlook

Clouds are fundamental to Earth's atmospheric dynamics, influencing radiation, precipitation, and heat transport. Despite their critical role in the planet's radiation budget and water cycle, clouds remain a major source of uncertainty in climate quantification, as highlighted by the IPCC (2014). The complexity of their mechanisms and microphysical properties, tied to local atmospheric conditions and aerosol particles, adds to this uncertainty. Aerosols impact radiation directly through scattering and absorption and indirectly by acting as cloud condensation nuclei (CCN) or ice nucleating particles (INP), influencing cloud formation and lifetime.
Given the variability of aerosol amounts and compositions, meteorological conditions, and cloud formation processes, studying clouds and aerosols within their environmental context is essential. Tajikistan's location within the dust belt, along with local and regional desertification, local pollution from traffic, industrial manufacturies and other anthropogenic sources, and glacier retreat, makes it significant for studying dust and non-dust aerosol particles and their atmospheric effects (e.g., Jiang et al., 2019; Goerlich et al., 2020; Hofer, 2020). The deployment of a new and upgraded permanent lidar station in 2019 (Engelmann et al., 2019; Jimenez, 2021), equipped with cloud measurement capabilities, has enabled continuous, long-term high-resolution measurements from 2019 to 2023. This thesis utilized data from this state-of-the-art ground-based lidar located in Dushanbe, Tajikistan, to investigate aerosol and liquid water cloud microphysical properties and their interactions. This research extends previous short-term studies and provides a comprehensive analysis of aerosol-cloud interactions in continental, dusty, and often polluted environments like Dushanbe.

The role of observational resolution to assess ACIs is an open aspect(McComiskey and Feingold, 2012). By exploiting the lidar capabilities,

in this thesis, aerosol and cloud properties were investigated across different time scales. Generally, higher N_{CCN} than N_{d} were observed in Dushanbe. Winter showed the lowest N_{d} with the highest R_{eff}, while summer showed the opposite. The strong aerosol presence likely makes cloud formation in Dushanbe to follow an updraft-limited regime, however a link between the aerosol and cloud properties was present among the different scales, although their covariability does not follow a 1:1 relation. In general, positive values for the ACI index were found, suggesting clouds follow rather a transitional regime, between aerosol-limited and updraft-limited. Higher N_{d} were observed during periods of lower atmospheric stability, but also stronger correlation to the aerosol properties was witnessed as well. The aerosol-cloud interactions were further examined by calculating the ACI index for various time periods. The length of the selected time period and the number of cloud occurrences significantly affected the ACI index, with higher cloud occurrences leading to generally a higher ACI index during less stable atmospheric conditions. From eight selected periods where the variability of single clouds was considered, ACI indexes at time scales from 1 to 10 weeks were found to vary between 0.197 to 1.256. From the monthly changes excluding winter time, an ACI index of about 0.325 and considered large averaging periods of several months, a clear ACI index of 0.549 was obtained. Suggesting a strong cloud response to aerosol, when considering large temporal scales. This highlights the need for further investigations into the scale problem when studying aerosol-cloud interactions and corroborates the potential of continuous lidar measurements to tackle the problem.

Given the fine resolution available, very short scales, of some minutes, were selected to investigate fast cloud responses to aerosol conditions using the high-resolution aerosol and cloud products. Aerosol particles were distinguished between dust and non-dust, and CCN number concentrations were estimated based on the POLIPHON method (Mamouri and Ansmann, 2016). All three case studies took place during relatively clean conditions with low dust contribution. The difference among the cases confirm the effect of atmospheric stability on cloud droplet activation, although within the periods a slight correlation between N_{d} and N_{CCN} could be seen. In general, it seems the assumed 0.2 % maximum supersaturation for the CCN retrieval is hardly reachable in this dry region. It was found that at less stable conditions N_{CCN} (at supersaturation of 0.2 %) and N_{d} were in closer ranges compared to stable situations where they showed the strongest contrast of at least one order of magnitude.

Seasonal analysis of the source regions where air masses resided before reaching Dushanbe provided further insights into the complexity of aerosol compositions in this region. Central Asia, Persia, and the Sahara were the

most influential regions throughout most seasons. These regions consist of many deserts that used to be covered by water, which can cause salty dust mixtures which could have potential on the hydroscopicity of dust aerosols. Similar findings from Hofer (2020) where low lidar ratios were measured along high particle depolarization ratios, which could be explained by salty dust mixtures emphasize the importance of future laboratory assessments of aerosol compositions based on in situ measurements, such as the OLALA campaign (OLALA, 2024).
Finally, for cross checking of new available data sets, comparisons of CCN number concentration estimates from ground-based lidar in Dushanbe, spaceborne lidar CALIOP, and CAMS reanalysis were compared and showed good agreement. However, differences between dust and non-dust contributions from ground-based and satellite-based observations require further investigation.

The findings from this thesis contribute to our understanding of aerosol-cloud interactions, particularly in continental, dusty, and often polluted environments like Dushanbe. The results highlight the importance of ongoing research in this field, particularly through ground-based lidar systems, which offer high temporal and vertical resolution measurements that complement satellite, airborne observations, and model-based research. This thesis underscores the critical role of meteorological conditions, e.g., turbulence and relative humidity, in influencing aerosols and their interactions with clouds. The temporal scale when investigating ACI significantly impacts the results, emphasizing the need for different scales to resolve aerosol-cloud interactions in detail. Continuous, long-term observations are essential for improving our understanding of atmospheric processes. The DFOV polarization lidar PollyXT at the observatory at the S.U. Umarov Physical Technical Institute, in partnership with the Leibniz Institute for Tropospheric Research, is one of the few experimental measurement sites in this region. The insights gained from this research in Dushanbe provide valuable contributions to the broader field of climate science and highlight the importance of experimental measurement approaches in addressing the complexities of aerosol-cloud interactions.

Appendix A

Uncertainties

Table A.1: Overview of uncertainties for cloud and aerosol products with the reference height z_{ref} , which is 75 m above the height of the cloud base, and R, the distance between the receiver of the lidar and the atmospheric component that scatters the laser light back. Based on Jimenez (2021) and Hofer (2020).

Parameter	**Symbol**	**Uncertainty**
Dust and non-dust backscatter coefficient	$\beta_{\mathrm{d}}(R)$, $\beta_{\mathrm{nd}}(R)$	20 %
Dust and non-dust extinction coefficient	$\alpha_{\mathrm{d}}(R)$, $\alpha_{\mathrm{nd}}(R)$	20 %
Volume depolarization ratio	$\delta_{\mathrm{vol}}(R)$	3–5 %
Particle depolarization ratio	$\delta_{\mathrm{par}}(R)$	5–10 %
Cloud base	$\mathrm{CB}(z_{\mathrm{ref}})$	0.1–1 %
Effective radius	$R_{\mathrm{eff}}(z_{\mathrm{ref}})$	15 %
Liquid water content	$LWC(z_{\mathrm{ref}})$	25 %
Cloud extinction coefficient	$\alpha_{\mathrm{c}}(z_{\mathrm{ref}})$	15–20 %
Cloud droplet number concentration	$N_{\mathrm{d}}(z_{\mathrm{ref}})$	25–75 %
Dust and non-dust CCN number concentration	$N_{\mathrm{CCN,d}}(R)$, $N_{\mathrm{CCN,nd}}(R)$	factor of 2
Aerosol-cloud interaction index	$E_{\mathrm{ACI}}^{N_{\mathrm{d}}}$	25–40 %

Bibliography

Abuduwaili, J., Liu, D., and Wu, G.: Saline dust storms and their ecological impacts in arid regions, J. Arid Land, 2, 144–150, doi:10.3724/SP.J.1227.2010.00144, 2010.

Abuduwaili, J., Issanova, G., and Saparov, G.: Hydrology and Limnology of Central Asia, Springer, doi:doi.org/10.1007/978-981-13-0929-8, 2018.

Ackerman, O., Kirkpatrick, M. P., Stevens, D. E., and Toon, O. B.: The impact of humidity above stratiform clouds on indirect aerosol climate forcing, Nature, 432, 1014–1017, doi:10.1038/nature03174, 2004.

Althausen, D., Engelmann, R., Foster, R., Rhone, P., and Baars, H.: Portable Raman LIDAR for determination of particle backscatter and extinction coefficients, in: Proceedings of the 22nd International Laser Radar Conference (ILRC 2004), edited by Pappalardo, G. and Amodeo, A., ESA SP-561, pp. 83–86, European Space Agency, 2004.

Althausen, D., Engelmann, R., Baars, H., Heese, B., Ansmann, A., Müller, D., and Komppula, M.: Portable Raman lidar Polly^{XT} for automated profiling of aerosol backscatter, extinction, and depolarization, J. Atmos. Ocean. Tech., 26, 2366–2378, doi:10.1175/2009JTECHA1304.1, 2009.

Ansmann, A., Riebesell, M. A., and Weitkamp, C.: Measurement of atmospheric aerosol extinction profiles with a Raman lidar, Opt. Lett., 15, 746–748, doi:10.1364/OL.15.000746, 1990.

Ansmann, A., Riebesell, M. A., Wandinger, U., Weitkamp, C., Voss, E., Lahmann, W., and Michaelis, W.: Combined raman elastic-backscatter LIDAR for vertical profiling of moisture, aerosol extinction, backscatter, and LIDAR ratio, App. Phys., 55, 18–28, doi:10.1007/BF00348608, 1992a.

Ansmann, A., Wandinger, U., Riebesell, M. A., Weitkamp, C., and Michaelis, W.: Independent measurement of extinction and backscatter profiles in

cirrus clouds by using a combined Raman elastic-backscatter lidar, Appl. Opt., 31, 7113–7131, doi:10.1364/AO.31.007113, 1992b.

Ansmann, A., Mamouri, R.-E., Hofer, J., Baars, H., Althausen, D., and Abdullaev, S. F.: Dust mass, cloud condensation nuclei, and ice-nucleating particle profiling with polarization lidar: updated POLIPHON conversion factors from global AERONET analysis, Atmos. Meas. Tech., 12, 4849–4865, doi:10.5194/amt-12-4849-2019, 2019.

Baars, H., Ansmann, A., Engelmann, R., and Althausen, D.: Continuous monitoring of the boundary-layer top with lidar, ACP, 8, 7281–7296, doi:10.5194/acp-8-7281-2008, 2008.

Baars, H., Kanitz, T., Engelmann, R., Althausen, D., Heese, B., Komppula, M., Preißler, J., Tesche, M., Ansmann, A., Wandinger, U., Lim, J.-H., Ahn, J. Y., Stachlewska, I. S., Amiridis, V., Marinou, E., Seifert, P., Hofer, J., Skupin, A., Schneider, F., Bohlmann, S., Foth, A., Bley, S., Pfüller, A., Giannakaki, E., Lihavainen, H., Viisanen, Y., Hooda, R. K., Pereira, S. N., Bortoli, D., Wagner, F., Mattis, I., Janicka, L., Markowicz, K. M., Achtert, P., Artaxo, P., Pauliquevis, T., Souza, R. A. F., Sharma, V. P., van Zyl, P. G., Beukes, J. P., Sun, J., Rohwer, E. G., Deng, R., Mamouri, R. E., and Zamorano, F.: An overview of the first decade of Polly^{NET}: an emerging network of automated Raman-polarization lidars for continuous aerosol profiling, Atmos. Chem. Phys., 16, 5111–5137, doi:10.5194/acp-16-5111-2016, 2016.

Baars, H., Seifert, P., Engelmann, R., and Wandinger, U.: Target categorization of aerosol and clouds by continuous multiwavelength-polarization lidar measurements, Atmos. Meas. Tech., 10, 3175–3201, doi:10.5194/amt-10-3175-2017, 2017.

Block, K., Haghighatnasab, M., Partridge, D. G., Stier, P., and Quaas, J.: Cloud condensation nuclei concentrations derived from the CAMS reanalysis, Earth Syst. Sci. Data, 16, 443–470, doi:10.5194/essd-16-443-2024, 2024.

Block(2023): Cloud condensation nuclei (CCN) numbers derived from CAMS reanalysis EAC4 (Version 1), WDC Climate [data set], doi:10.26050/WDCC/QUAERERE_CCNCAMS_v1, 2023.

Bucholtz, A.: Rayleigh-scattering calculations for the terrestrial atmosphere, Appl. Opt., 34, 2765–2773, doi:10.1364/AO.34.002765, 1995.

Chen, L., Peng, C., Gu, W., Fu, H., Jian, X., Zhang, H., Zhang, G., Zhu, J., Wang, X., and Tang, M.: On mineral dust aerosol hygroscopicity, ACP, 20, 13 611–13 626, doi:10.5194/acp-20-13611-2020, 2020.

Choudhury, G. and Tesche, M.: Estimating cloud condensation nuclei concentrations from CALIPSO lidar measurements, Atmos. Meas. Tech., 15, 639–654, doi:10.5194/amt-15-639-2022, 2022a.

Choudhury, G. and Tesche, M.: Assessment of CALIOP-derived CCN concentrations by in situ surface measurements, Remote Sens., 14, 3342, doi:10.3390/rs14143342, 2022b.

Choudhury, G. and Tesche, M.: A first global height-resolved cloud condensation nuclei data set derived from spaceborne lidar measurements, Earth Syst. Sci. Data, 15, 3747–3760, doi:10.5194/essd-15-3747-2023, 2023a.

Choudhury, G. and Tesche, M.: Global multiyear 3D dataset of cloud condensation nuclei derived from spaceborne lidar measurements, doi:10.1594/PANGAEA.956215, 2023b.

Choudhury, G., Ansmann, A., and Tesche, M.: Evaluation of aerosol number concentrations from CALIPSO with ATom airborne in situ measurements, Atmos. Chem. Phys., 22, 7143–7161, doi:10.5194/acp-22-7143-2022, 2022.

Dubovik, O. and King, M. D.: A flexible inversion algorithm for retrieval of aerosol optical properties from Sun and sky radiance measurements, J. Geophys. Res. Atmos., 105, 20 673–20 696, doi:10.1029/2000JD900282, 2000.

Dubovik, O., Sinyuk, A., Lapyonok, T., Holben, B., Mishchenko, M., Yang, P., Eck, T. F., Volten, H., Muñoz, O., Veihelmann, B., van der Zande, W. J., Leon, J.-F., Sorokin, M., and Slutsker, I.: Application of spheroid models to account for aerosol particle nonsphericity in remote sensing of desert dust, J. Atmos. Sci., 59, 590–608, doi:10.1175/1520-0469(2002)0592.0.CO;2, 2006.

Engelmann, R., Kanitz, T., Baars, H., Heese, B., Althausen, D., Skupin, A., Wandinger, U., Komppula, M., Stachlewska, I. S., Amiridis, V., Marinou, E., Mattis, I., Linné, H., and Ansmann, A.: The automated multiwavelength Raman polarization and water-vapor lidar Polly^{XT}: the neXT generation, Atmos. Meas. Tech., 9, 1767–1784, doi:10.5194/amt-9-1767-2016, 2016.

Engelmann, R., Hofer, J., Makhmudov, A. N., Baars, H., Hanbuch, K., Ansmann, A., Abdullaev, S. F., Macke, A., and Althausen, D.: CADEX and beyond: Installation of a new Polly^{XT} site in Dushanbe, in: Proc. Central Asian Dust Conference (CADUC), Dushanbe, Tajikistan, doi:10.1051/e3sconf/20199902010, 2019.

Floutsi, A. A., Baars, H., Radenz, M., Haarig, M., Yin, Z., Seifert, P., Jimenez, C., Ansmann, A., Engelmann, R., Barja, B., Zamorano, F., and Wandinger, U.: Advection of biomass burning aerosols towards the Southern Hemispheric mid-latitude station of Punta Arenas as observed with multiwavelength polarization Raman lidar, Remote Sens., 13, 138, doi:10.3390/rs13010138, 2021.

Freudenthaler, V.: About the effects of polarising optics on lidar signals and the $\Delta 90$ calibration, Atmos. Meas. Tech., 9, 4181–4255, doi:10.5194/amt-9-4181-2016, 2016.

Freudenthaler, V., Esselborn, M., Wiegner, M., Heese, B., Tesche, M., Ansmann, A., Müller, D., Althausen, D., Wirth, M., Fix, A., Ehret, G., Knippertz, P., Toledano, C., Gasteiger, J., Garhammer, M., and Seefeldner, M.: Depolarization ratio profiling at several wavelengths in pure Saharan dust during SAMUM 2006, Tellus B, 61, 165–179, doi:10.1111/j.1600-0889.2008.00396.x, 2009.

Freudenthaler, V., Linné, H., Chaikovski, A., Rabus, D., and Groß, S.: EARLINET lidar quality assurance tools, Atmos. Meas. Tech. Discuss., 2018, 1–35, doi:10.5194/amt-2017-395, 2018.

Gan, Y., Zhang, Z., Liu, F., Chen, Z., Guo, Q., Zhu, Z., and Ren, Y.: Analysis of characteristics and changes in three-dimensional spatial and temporal distribution of aerosol types in Central Asia, Sci. Total Environ., 927, 172 196, doi:https://doi.org/10.1016/j.scitotenv.2024.172196, 2024.

GDAS(2024): Global Data Assimilation System, meteorological data base, available at: `https://www.ready.noaa.gov/gdas1.php`, 2023.

Goerlich, F., Bolch, T., and Paul, F.: More dynamic than expected: an updated survey of surging glaciers in the Pamir, Earth Syst. Sci. Data, 12, 3161–3176, doi:10.5194/essd-12-3161-2020, 2020.

Gryspeerdt, E., Goren, T., Sourdeval, O., Quaas, J., Mülmenstädt, J., Dipu, S., Unglaub, C., Gettelman, A., and Christensen, M.: Constraining the aerosol influence on cloud liquid water path, Atmos. Chem. Phys., 19, 5331–5347, doi:10.5194/acp-19-5331-2019, 2019.

Han, Y., Wang, T., Tan, R., Tang, J., Wang, C., He, S., Dong, Y., Huang, Z., and Bi, J.: CALIOP-based quantification of Central Asian dust transport, Remote Sens., 14, 1416, doi:10.3390/rs14061416, 2022.

Hasekamp, O. P., Gryspeerdt, E., and Quaas, J.: Analysis of polarimetric satellite measurements suggests stronger cooling due to aerosol-cloud interactions, Nat. Commun., 10, 5405, doi:10.1038/s41467-019-13372-2, 2019.

Heyn, I., Block, K., Mülmenstädt, J., Gryspeerdt, E., Kühne, P., Salzmann, M., and Quaas, J.: Assessment of simulated aerosol effective radiative forcings in the terrestrial spectrum, Geophys. Res. Lett., 44, 1001–1007, doi:10.1002/2016GL071975, 2017.

Hofer, J.: Aerosol characterization over a Central Asian site: long-term lidar profiling at Dushanbe, Tajikistan (March 2015 – August 2016), Ph.D. thesis, University of Leipzig, URL `https://nbn-resolving.org/urn:nbn:de:bsz:15-qucosa2-724615`, 2020.

Hofer, J., Althausen, D., Abdullaev, S. F., Makhmudov, A. N., Nazarov, B. I., Schettler, G., Engelmann, R., Baars, H., Fomba, K. W., Müller, K., Heinold, B., Kandler, K., and Ansmann, A.: Long-term profiling of mineral dust and pollution aerosol with multiwavelength polarization Raman lidar at the Central Asian site of Dushanbe, Tajikistan: case studies, Atmos. Chem. Phys., 17, 14 559–14 577, doi:10.5194/acp-17-14559-2017, 2017.

Hofer, J., Ansmann, A., Althausen, D., Engelmann, R., Baars, H., Abdullaev, S. F., and Makhmudov, A. N.: Long-term profiling of aerosol light extinction, particle mass, cloud condensation nuclei, and ice-nucleating particle concentration over Dushanbe, Tajikistan, in Central Asia, Atmos. Chem. Phys., 20, 4695–4711, doi:10.5194/acp-20-4695-2020, 2020a.

Hofer, J., Ansmann, A., Althausen, D., Engelmann, R., Baars, H., Fomba, K. W., Wandinger, U., Abdullaev, S. F., and Makhmudov, A. N.: Optical properties of Central Asian aerosol relevant for spaceborne lidar applications and aerosol typing at 355 and 532 nm, Atmos. Chem. Phys., 20, 9265–9280, doi:10.5194/acp-20-9265-2020, 2020b.

Hofer, J., Althausen, D., Ansmann, A., Abdullaev, S. F., Makhmudov, A. N., Lipken, F., Jimenez, J., Baars, H., Engelmann, R., and Radenz, M.: Low lidar ratios at elevated depolarization ratios in Dushanbe - Revisited using a time–height resolved air mass source attribution tool, in: E3S Web Conf., Proc. 2nd Central Asian Dust Conference (CADUC-2), Nukus, Uzbekistan, 2024a.

Hofer, J., Seifert, P., Liley, J. B., Radenz, M., Uchino, O., Morino, I., Sakai, T., Nagai, T., and Ansmann, A.: Aerosol-related effects on the occurrence of heterogeneous ice formation over Lauder, New Zealand / Aotearoa, Atmos. Chem. Phys., 24, 1265–1280, doi:10.5194/acp-24-1265-2024, 2024b.

Holben, B. N., Eck, T. F., Slutsker, I., Tanré, D., Buis, J. P., Setzer, A., Vermote, E., Reagan, J. A., Kaufman, Y. J., Nakajima, T., Lavenu, F., Jankowiak, I., and Smirnov, A.: AERONET - A federated instrument network and data archive for aerosol characterization, Remote Sens. Environ., 66, 1–16, doi:10.1016/S0034-4257(98)00031-5, 1998.

Holben, B. N., Tanré, D., Smirnov, A., Eck, T. F., Slutsker, I., Abuhassan, N., Newcomb, W. W., Schafer, J. S., Chatenet, B., Lavenu, F., Kaufman, Y. J., Castle, J. V., Setzer, A., Markham, B., Clark, D., Frouin, R., Halthore, R., Karneli, A., O'Neill, N. T., Pietras, C., Pinker, R. T., Voss, K., and Zibordi, G.: An emerging ground-based aerosol climatology: aerosol optical depth from AERONET, J. Geophys. Res. Atmos., 106, 12 067–12 097, doi:10.1029/2001JD900014, 2001.

Huang, T., Zhu, Y., Rosenfeld, D., Yang, Y., Lam, D. H. Y., Leung, W. H., Lee, H. F., Cheng, J. C. H., and Yim, S. H. L.: Regime-dependent impacts of aerosol particles and updrafts on the cloud condensation nuclei and the enhanced warm rain suppression: evidence from synergistic satellite and LiDAR observations, Geophys. Res. Lett., 49, e2021GL097 315, doi:10.1029/2021GL097315, 2022.

Illingworth, A. J., Hogan, R. J., O'Connor, E., Bouniol, D., Brooks, M. E., Delanoé, J., Donovan, D. P., Eastment, J. D., Gaussiat, N., Goddard, J. W. F., Haeffelin, M., Klein Baltink, H., Krasnov, O. A., Pelon, J., Piriou, J.-M., Protat, A., Russchenberg, H. W. J., Seifert, A., Tompkins, A. M., van Zadelhoff, G.-J., Vinit, F., Willén, U., Wilson, D. R., and Wrench, C. L.: Cloudnet: continuous evaluation of cloud profiles in seven operational models using ground-based observations, Bull. Am. Meteorol. Soc., 88, 883–898, doi:10.1175/BAMS-88-6-883, 2007.

Inness, A., Ades, M., Agustí-Panareda, A., Barré, J., Benedictow, A., Blechschmidt, A.-M., Dominguez, J. J., Engelen, R., Eskes, H., Flemming, J., Huijnen, V., Jones, L., Kipling, Z., Massart, S., Parrington, M., Peuch, V.-H., Razinger, M., Remy, S., Schulz, M., and Suttie, M.: The CAMS reanalysis of atmospheric composition, Atmos. Chem. Phys., 19, 3515–3556, doi:10.5194/acp-19-3515-2019, 2019.

IPCC: Climate Change 2014: Synthesis Report. Contribution of Working Groups I, II and III to the Fifth Assessment Report of the Intergovernmental Panel on Climate Change, edited by: Core Writing Team, Pachauri, R. K., and Meyer, L. A., IPCC, URL https://www.ipcc.ch/report/ar5/syr/, 2014.

Jiang, L., Jiapaer, G., Bao, A., Kurban, A., Guo, H., Zheng, G., and De Maeyer, P.: Monitoring the long-term desertification process and assessing the relative roles of its drivers in Central Asia, Ecol. Indic., 104, 195–208, doi:https://doi.org/10.1016/j.ecolind.2019.04.067, 2019.

Jimenez, C.: Observations of aerosol and liquid-water clouds with Dual-Field-of-View Polarization Lidar, Ph.D. thesis, University of Leipzig, URL https://nbn-resolving.org/urn:nbn:de:bsz:15-qucosa2-769056, 2021.

Jimenez, C., Ansmann, A., Engelmann, R., Donovan, D., Malinka, A., Schmidt, J., Seifert, P., and Wandinger, U.: The dual-field-of-view polarization lidar technique: a new concept in monitoring aerosol effects in liquid-water clouds – theoretical framework, Atmos. Chem. Phys., 20, 15 247–15 263, doi:10.5194/acp-20-15247-2020, 2020a.

Jimenez, C., Ansmann, A., Engelmann, R., Donovan, D., Malinka, A., Seifert, P., Wiesen, R., Radenz, M., Yin, Z., Bühl, J., Schmidt, J., Barja, B., and Wandinger, U.: The dual-field-of-view polarization lidar technique: a new concept in monitoring aerosol effects in liquid-water clouds – case studies, Atmos. Chem. Phys., 20, 15 265–15 284, doi:10.5194/acp-20-15265-2020, 2020b.

Laj, P., Lund Myhre, C., Riffault, V., Amiridis, V., Fuchs, H., Eleftheriadis, K., Petäjä, T., Salameh, T., Kivekäs, N., Juurola, E., Saponaro, G., Philippin, S., Cornacchia, C., Arboledas, L., Baars, H., Claude, A., De Mazière, M., Dils, B., Dufresne, M., Evangeliou, N., Favez, O., Fiebig, M., Haeffelin, M., Herrmann, H., Höhler, K., Illmann, N., Kreuter, A., Ludewig, E., Marinou, E., Möhler, O., Mona, L., Murberg, L., Nicolae, D., Novelli, A., O'Connor, E., Ohneiser, K., Petracca Altieri, R., Picquet-Varrault, B., van Pinxteren, D., Pospichal, B., Putaud, J., Reimann, S., Siomos, N., Stachlewska, I., Tillmann, R., Voudouri, K., Wandinger, U., Wiedensohler, A., Apituley, A., Comerón, A., Gysel-Beer, M., Mihalopoulos, N., Nikolova, N., Pietruczuk, A., Sauvage, S., Sciare, J., Skov, H., Svendby, T., Swietlicki, E., Tonev, D., Vaughan, G., Zdimal, V., Baltensperger, U., Doussin, J., Kulmala, M., Pappalardo, G., Sundet, S., and Vana, M.:

Aerosol, Clouds and Trace Gases Research Infrastructure ACTRIS, the European research infrastructure supporting atmospheric science, Bull. Am. Meteorol. Soc., doi:10.1175/BAMS-D-23-0064.1, 2024.

Li, L. and Sokolik, I. N.: Analysis of Dust Aerosol Retrievals Using Satellite Data in Central Asia, Atmosphere, 9, doi:10.3390/atmos9080288, 2018.

Lipken, F., Hofer, J., Jimenez, C., Althausen, D., Radenz, M., Engelmann, R., Baars, H., and Abdullaev, S. F.: Relating cloud and aerosol properties from long-term lidar observations in Tajikistan, in: E3S Web Conf., Proc. 2nd Central Asian Dust Conference (CADUC-2), Nukus, Uzbekistan, 2024.

Liu, Y., Zhu, Q., Wang, R., Xiao, K., and Cha, P.: Distribution, source and transport of the aerosols over Central Asia, Atmos. Environ., 210, 120–131, doi:10.1016/j.atmosenv.2019.04.052, 2019.

Lohmann, U., Lüönd, F., and Mahrt, F.: An Introduction to Clouds: From the Microscale to Climate, Cambridge University Press, doi:10.1017/cbo9781139087513, 2016.

Lv, M., Wang, Z., Li, Z., Luo, T., Ferrare, R., Liu, D., Wu, D., Mao, J., Wan, B., Zhang, F., and Wang, Y.: Retrieval of cloud condensation nuclei number concentration profiles from lidar extinction and backscatter data, J. Geophys. Res. Atmos., 123, 6082–6098, doi:10.1029/2017JD028102, 2018.

Mamouri, R., Nisantzi, A., Engelmann, R., Buehl, J., Seifert, P., Baars, H., Yin, Z., Hadjimitsis, D., and Ansmann, A.: The ERATOSTHENES CoE in the PollyNET:First observations of the PollyXT-CYP at Limassol, Cyprus, in: EGU General Assembly Conference Abstracts, EGU General Assembly Conference Abstracts, p. 16279, doi:10.5194/egusphere-egu21-16279, 2021.

Mamouri, R.-E. and Ansmann, A.: Potential of polarization lidar to provide profiles of CCN- and INP-relevant aerosol parameters, Atmos. Chem. Phys., 16, 5905–5931, doi:10.5194/acp-16-5905-2016, 2016.

Martin, G. M., Johnson, D. W., and Spice, A.: The measurement and parameterization of effective radius of droplets in warm stratocumulus clouds, J. Atmos. Sci., 51, 1823–1842, doi:10.1175/1520-0469(1994)051<1823:TMAPOE>2.0.CO;2, 1994.

Masonis, S. J., Anderson, T. L., Covert, D. S., Kapustin, V., Clarke, A. D., Howell, S., and Moore, K.: A study of the extinction-to-backscatter ratio of marine aerosol during the Shoreline Environment

Aerosol Study, J. Atmos. Ocean. Tech., 20, 1388–1402, doi:10.1175/1520-0426(2003)020<1388:ASOTER>2.0.CO;2, 2003.

Mattis, I., Tesche, M., Grein, M., Freudenthaler, V., and Müller, D.: Systematic error of lidar profiles caused by a polarization-dependent receiver transmission: quantification and error correction scheme, Appl. Opt., 48, 2742–2751, doi:10.1364/AO.48.002742, 2009.

McComiskey, A. and Feingold, G.: The scale problem in quantifying aerosol indirect effects, Atmos. Chem. Phys., 12, 1031–1049, doi:10.5194/acp-12-1031-2012, 2012.

Molod, A., Takacs, L., Suarez, M., and Bacmeister, J.: Development of the GEOS-5 atmospheric general circulation model: evolution from MERRA to MERRA2, Geosci. Model Dev., 8, 1339–1356, doi:10.5194/gmd-8-1339-2015, 2015.

Müller, D., Ansmann, A., Mattis, I., Tesche, M., Wandinger, U., Althausen, D., and Pisani, G.: Aerosol-type-dependent lidar ratios observed with Raman lidar, J. Geophys. Res. Atmos., 112, D16 202, doi:10.1029/2006JD008292, 2007.

Novakov, T. and Penner, J.: Large contribution of organic aerosols to could-condensation nuclei concentration, Nature, 365, 823–826, doi:10.1038/365823a0, 1993.

OLALA(2024): Optical Lab for Lidar Applications (OLALA), url: `https://www.tropos.de/en/institute/departments/remote-sensing-of-atmospheric-processes-new/ground-based-remote-sensing/olala`, 2024.

Omar, A. H., Won, J.-G., Winker, D. M., Yoon, S.-C., Dubovik, O., and McCormick, M. P.: Development of global aerosol models using cluster analysis of Aerosol Robotic Network (AERONET) measurements, J. Geophys. Res. Atmos., 110, doi:10.1029/2004JD004874, 2005.

Omar, A. H., Winker, D. M., Vaughan, M. A., Hu, Y., Trepte, C. R., Ferrare, R. A., Lee, K., Hostetler, C. A., Kittaka, C., Rogers, R. R., Kuehn, R. E., and Liu, Z.: The CALIPSO automated aerosol classification and lidar ratio selection algorithm, J. Atmos. Ocean. Tech., 26, 1994–2014, doi:10.1175/2009JTECHA1231.1, 2009.

Pappalardo, G., Amodeo, A., Apituley, A., Comeron, A., Freudenthaler, V., Linné, H., Ansmann, A., Bösenberg, J., D'Amico, G., Mattis, I., Mona,

L., Wandinger, U., Amiridis, V., Alados-Arboledas, L., Nicolae, D., and Wiegner, M.: EARLINET: towards an advanced sustainable European aerosol lidar network, Atmos. Meas. Tech., 7, 2389–2409, doi:10.5194/amt-7-2389-2014, 2014.

Pisso, I., Sollum, E., Grythe, H., Kristiansen, N. I., Cassiani, M., Eckhardt, S., Arnold, D., Morton, D., Thompson, R. L., Groot Zwaaftink, C. D., Evangeliou, N., Sodemann, H., Haimberger, L., Henne, S., Brunner, D., Burkhart, J. F., Fouilloux, A., Brioude, J., Philipp, A., Seibert, P., and Stohl, A.: The Lagrangian particle dispersion model FLEXPART version 10.4, Geosci. Model Dev., 12, 4955–4997, doi:10.5194/gmd-12-4955-2019, 2019.

Quaas, J., Boucher, O., and Lohmann, U.: Constraining the total aerosol indirect effect in the LMDZ and ECHAM4 GCMs using MODIS satellite data, Atmos. Chem. Phys., 6, 947–955, doi:10.5194/acp-6-947-2006, 2006.

Quaas, J., Boucher, O., Bellouin, N., and Kinne, S.: Satellite-based estimate of the direct and indirect aerosol climate forcing, J. Geophys. Res. Atmos., 113, doi:10.1029/2007JD008962, 2008.

Quaas, J., Jia, H., Smith, C., Albright, A. L., Aas, W., Bellouin, N., Boucher, O., Doutriaux-Boucher, M., Forster, P. M., Grosvenor, D., Jenkins, S., Klimont, Z., Loeb, N. G., Ma, X., Naik, V., Paulot, F., Stier, P., Wild, M., Myhre, G., and Schulz, M.: Robust evidence for reversal of the trend in aerosol effective climate forcing, Atmos. Chem. Phys., 22, 12 221–12 239, doi:10.5194/acp-22-12221-2022, 2022.

Radenz, M., Bühl, J., Seifert, P., Baars, H., Engelmann, R., Barja González, B., Mamouri, R.-E., Zamorano, F., and Ansmann, A.: Hemispheric contrasts in ice formation in stratiform mixed-phase clouds: disentangling the role of aerosol and dynamics with ground-based remote sensing, Atmos. Chem. Phys., 21, 17 969–17 994, doi:10.5194/acp-21-17969-2021, 2021a.

Radenz, M., Seifert, P., Baars, H., Floutsi, A. A., Yin, Z., and Bühl, J.: Automated time–height-resolved air mass source attribution for profiling remote sensing applications, Atmos. Chem. Phys., 21, 3015–3033, doi:10.5194/acp-21-3015-2021, 2021b.

Reutter, P., Su, H., Trentmann, J., Simmel, M., Rose, D., Gunthe, S. S., Wernli, H., Andreae, M. O., and Pöschl, U.: Aerosol- and updraft-limited regimes of cloud droplet formation: influence of particle number, size and

hygroscopicity on the activation of cloud condensation nuclei (CCN), Atmos. Chem. Phys., 9, 7067–7080, doi:10.5194/acp-9-7067-2009, 2009.

Rosenfeld, D., Andreae, M. O., Asmi, A., Chin, M., de Leeuw, G., Donovan, D. P., Kahn, R., Kinne, S., Kivekäs, N., Kulmala, M., Lau, W., Schmidt, K. S., Suni, T., Wagner, T., Wild, M., and Quaas, J.: Global observations of aerosol-cloud-precipitation-climate interactions, Rev. Geophys., 52, 750–808, doi:10.1002/2013RG000441, 2014.

Rupakheti, D., Kang, S., Bilal, M., Gong, J., Xia, X., and Cong, Z.: Aerosol optical depth climatology over Central Asian countries based on Aqua-MODIS Collection 6.1 data: Aerosol variations and sources, Atmos. Environ., 207, 205–214, doi:https://doi.org/10.1016/j.atmosenv.2019.03.020, 2019.

Schmidt, J., Wandinger, U., and Malinka, A.: Dual-field-of-view Raman lidar measurements for the retrieval of cloud microphysical properties, Appl. Opt., 52, 2235–2247, doi:10.1364/AO.52.002235, 2013.

Shukurov, K. A., Simonenkov, D. V., Nevzorov, A. V., Rashki, A., Hamzeh, N. H., Abdullaev, S. F., Shukurova, L. M., and Chkhetiani, O. G.: CALIOP-Based Evaluation of Dust Emissions and Long-Range Transport of the Dust from the AralCaspian Arid Region by 3D-Source Potential Impact (3D-SPI) Method, J. Rem. Sens., 15, doi:10.3390/rs15112819, 2023.

Siebert, H. and Shaw, R. A.: Supersaturation fluctuations during the early stage of cumulus formation, J. Atmos. Sci., 74, 975–988, doi:10.1175/JAS-D-16-0115.1, 2017.

Singer, A., Zobeck, T., Poberezsky, L., and Argaman, E.: The PM10and PM2·5 dust generation potential of soils/sediments in the Southern Aral Sea Basin, Uzbekistan, J. Arid Environ., 54, 705–728, doi:https://doi.org/10.1006/jare.2002.1084, 2003.

Stein, A. F., Draxler, R. R., Rolph, G. D., Stunder, B. J. B., Cohen, M. D., and Ngan, F.: NOAA's HYSPLIT atmospheric transport and dispersion modeling system, Bull. Am. Meteorol. Soc., 96, 2059–2077, doi:10.1175/BAMS-D-14-00110.1, 2015.

Stohl, A., Forster, C., Frank, A., Seibert, P., and Wotawa, G.: Technical note: The Lagrangian particle dispersion model FLEXPART version 6.2., Atmos. Chem. Phys., 5, 2461–2474, doi:10.5194/acp-5-2461-2005, 2005.

Stokes, G. M. and Schwartz, S. E.: The Atmospheric Radiation Measurement (ARM) program: programmatic background and design of the cloud and radiation test bed, Bull. Am. Meteorol. Soc., 75, 1201–1222, doi:10.1175/1520-0477(1994)075<1201:TARMPP>2.0.CO;2, 1994.

Stull, R. B.: Practical Meteorology: An Algebra-based Survey of Atmospheric Science - version 1.02b, University of British Columbia, `https://www.eoas.ubc.ca/books/Practical_Meteorology/`, 2017.

Tesche, M., Ansmann, A., Müller, D., Althausen, D., Engelmann, R., Freudenthaler, V., and Groß, S.: Vertically resolved separation of dust and smoke over Cape Verde by using multiwavelength Raman and polarization lidars during Saharan Mineral Dust Experiment 2008, J. Geophys. Res. Atmos., 114, D13 202, doi:10.1029/2009JD011862, 2009.

Twomey, S.: The nuclei of natural cloud formation part II: The supersaturation in natural clouds and the variation of cloud droplet concentration, Geofis. Pura Appl., 43, 243–249, doi:10.1007/BF01993560, 1959.

Twomey, S.: Pollution and the planetary albedo, Atmos. Environ., 8, 1251–1256, doi:10.1016/0004-6981(74)90004-3, 1974.

Twomey, S.: Influence of pollution on shortwave albedo of clouds, J. Atmos., Sci., 34, 1149–1152, doi:10.1175/1520-0469(1977)034<1149:TIOPOT>2.0.CO;2, 1977.

Uin, J., Aiken, A. C., K., D. M., Kuang, C., Pekour, M., Salwen, C., Sedlacek, A. J., Senum, G., Smith, S., Wang, J., Watson, T. B., and Springston, S. R.: Atmospheric Radiation Measurement (ARM) Aerosol Observing Systems (AOS) for surface-based in situ atmospheric aerosol and trace gas measurements, J. Atmos. Ocean. Tech., 36, 2429–2447, doi:10.1175/JTECH-D-19-0077.1, 2019.

Voigt, A., Albern, N., Ceppi, P., Grise, K., Li, Y., and Medeiros, B.: Clouds, radiation, and atmospheric circulation in the present-day climate and under climate change, WIREs Climate Change, 12, 694, doi:https://doi.org/10.1002/wcc.694, 2021.

Wandinger, U. and Ansmann, A.: Experimental determination of the lidar overlap profile with Raman lidar, Appl. Opt., 41, 511–514, doi:10.1364/AO.41.000511, 2002.

Wandinger, U., Nicolae, D., Pappalardo, G., Mona, L., and Comerón, A.: ACTRIS and its aerosol remote sensing component, EPJ Web Conf., 237, 05 003, doi:10.1051/epjconf/202023705003, 2020.

Wang, D., Zhang, F., Yang, S., Xia, N., and Ariken, M.: Exploring the spatial-temporal characteristics of the aerosol optical depth (AOD) in Central Asia based on the moderate resolution imaging spectroradiometer (MODIS), Environ. Monit. Assess., 192, doi:10.1007/s10661-020-08299-x, 2020.

Weitkamp, C., ed.: Lidar: Range-Resolved Optical Remote Sensing of the Atmosphere, Springer, doi:10.1007/b106786, 2005.

Werner, F., Ditas, F., Siebert, H., Simmel, M., Wehner, B., Pilewskie, P., Schmeissner, T., Shaw, R. A., Hartmann, S., Wex, H., Roberts, G. C., and Wendisch, M.: Twomey effect observed from collocated microphysical and remote sensing measurements over shallow cumulus, J. Geophys. Res. Atmos., 119, 1534–1545, doi:10.1002/2013JD020131, 2014.

Winker, D. M., Vaughan, M. A., Omar, A., Hu, Y., Powell, K. A., Liu, Z., Hunt, W. H., and Young, S. A.: Overview of the CALIPSO mission and CALIOP data processing algorithms, J. Atmos. Ocean. Tech., 26, 2310–2323, doi:10.1175/2009JTECHA1281.1, 2009.

Wu, N., Ge, Y., Abuduwaili, J., Issanova, G., , and Saparov, G.: Insights into variations and potential long-range transport of atmospheric aerosols from the Aral Sea basin in Central Asia, Remote Sens., 14, 2310–2323, doi:10.3390/rs14133201, 2022.

Statement of authorship

I declare that I completed this thesis on my own and that information which has been directly or indirectly taken from other sources has been noted as such. Neither this nor a similar work has been presented to an examination committee.

Leipzig, 28 May 2024 .....